

Localizing Retinal Blood Vessels In Fundus Images using Fuzzy Logic Approach

by

Maryam Parhizkar

A thesis submitted to the Faculty of Graduate and Postdoctoral
Affairs in partial fulfilment of the requirements for the degree of

Master of Applied Science

in

Biomedical Engineering

Carleton University

Ottawa, Ontario

© 2022

Maryam Parhizkar

Abstract

The condition of the vascular system is crucial in the diagnosis of vision abnormalities. The essential element of computerized retinal analysis is vasculature segmentation in digital fundus images. This work introduces an automatic algorithm based on fuzzy logic to detect the retinal blood vessels. The methodology uses the green channel of images and employs pre-processing techniques. The features are extracted using the Robinson compass mask. The Mamdani interval type-2 fuzzy rules are applied to these features to detect the blood vessels, and the result is binarized, followed by post-processing refinements to maximize the performance.

The methodology is evaluated using the publicly available DRIVE (Digital Retinal Images for Vessel Extraction) database, and the results are compared with distinguished published methods. Achieving the average accuracy of 94.89%, the sensitivity of 74.78% and specificity of 96.85% show promising results for pre-screening treatments, while the technique could be extended to other image segmentation applications.

Acknowledgements

I would like to express my sincere gratitude to my advisor Dr. Jurek Sasiadek for his continuous support through this journey, whose guidance and feedback throughout the project paved the way for me to undertake this research.

I am also thankful to the Department of Aerospace and Mechanical Engineering and Ottawa-Carleton Institute for Biomedical Engineering, and all members' staff for thoughtful guidance.

Furthermore, I would like to thank my husband, whose generous support, advice, faith and love made me pursue my true passion.

Table of Contents

Abstract.....	ii
Acknowledgements.....	iii
List of Tables	viii
List of Figures.....	ix
List of Appendices	xiv
Abbreviations.....	xv
Chapter 1: Introduction.....	1
1.1. Human Visual System.....	1
1.2. Retinal Diseases	3
1.2.1. Diabetes and Diabetic Retinopathy.....	3
1.2.2. Retinopathy Of Prematurity (ROP)	5
1.3. Digital Fundus Photography.....	6
1.4. Motivation	7
1.5. Objectives.....	8
1.6. Thesis Formation.....	9

Chapter 2: Literature Review	11
2.1. Supervised Methods	12
2.2. Unsupervised Rule-Based Methods	16
Chapter 3: Methodology	22
3.1. Pre-processing	25
3.1.1. Green Channel Extraction.....	25
3.1.2. Contrast-Limited Adaptive Histogram Equalization (CLAHE)	27
3.1.3. Median Filter and Background Removal	30
3.1.4. Gaussian Filtering	33
3.1.5. Retina Area Extraction.....	34
3.1.6. Matched Filtering.....	36
3.2. Feature Extraction	42
3.3. Introduction to Fuzzy Logic Systems	47
3.3.1. The Motivation for Proposing a Fuzzy Logic System	47
3.3.2. Type-1 Fuzzy Inference System	49
3.3.3. Type-1 Fuzzy Membership Functions (MF).....	49
3.3.4. Linguistic Variables and Fuzzification	51
3.3.5. Fuzzy Rules.....	52

3.3.6.	Inference Engine	52
3.3.7.	Defuzzifier	53
3.3.8.	Generalized Type-2 Fuzzy System (GT2 FS).....	54
3.3.9.	Interval Type-2 Fuzzy System (IT2 FS)	57
3.4.	Proposed Fuzzy Logic Algorithm	60
3.5.	Post-processing.....	65
3.5.1.	Image Binarization.....	65
3.5.2.	Morphological Discovery	67
3.5.3.	Connected Component Analysis.....	71
Chapter 4: Simulation Results		74
4.1.	Database	74
4.2.	Performance Measures	75
4.2.1.	Confusion Matrix	75
4.2.2.	Quality Measurement Using MSE and PSNR Indices.....	78
4.3.	Simulation Results.....	79
4.4.	Model Evaluation	80
Chapter 5: Discussion		82

5.1. Evaluating the results	82
5.2. Summary of the work.....	92
5.2. Strengths and Weaknesses	93
5.3. Future Work	94
Chapter 6: Conclusion.....	96
References.....	98
Appendix.....	111
Appendix 1: Methodology MATLAB Code.....	111

List of Tables

TABLE 1: Designed Fuzzy Rules for the IT2 fuzzy system	64
TABLE 2: Performance results on DRIVE test data	79
TABLE 3: Descriptive statistics on the performance measures reported in Table 2.....	80
TABLE 4: Comparison between the proposed method and related works in terms of average values of accuracy, sensitivity and specificity	81
TABLE 5: The performance comparison of [20] and the proposed model in terms of Dice and Jaccard indices	88

List of Figures

Figure 1: Indication of the human eye structure [61].	2
Figure 2: Comparison of retinal blood vessels in regular and DR patients [63].....	4
Figure 3: (a) Central vessel reflex and poor contrast, (b) cotton-wool patches, (c) Hard exudates, (d) Retina anatomical structures [64].....	5
Figure 4: Retina examination using Canon digital fundus imaging system [59].	7
Figure 5: A flowchart of the proposed method.....	24
Figure 6: Visualization of a color digital fundus image and individual RGB channels from the DRIVE dataset	26
Figure 7: Illustration of (a) the grayscale image and (b) the green channel of an RGB image from the DRIVE dataset.....	27
Figure 8: Comparison of standard histogram equalization (HE) and Contrast-Limited Adaptive Histogram Equalization (CLAHE). Top row: (a) Green channel of an image from DRIVE test data, (b) Enhanced image using HE processing, (c) Contrast-improved image using CLAHE processing. Bottom row: The histograms of the corresponding images (a,b,c) are visualized. Results show that applying the CLAHE method makes the blood vessels more apparent while the noise is less amplified.	29

Figure 9: Estimated background using (a) median filter and (b) moving-average filter. Results show the moving-average filter shades of blood vessels through the estimated image..... 32

Figure 10: Background exclusion process. (a) Contrast-enhanced image by CLAHE, (b) Median filtered image, (c) Subtraction of ‘b’ from ‘a’ 32

Figure 11: (a) Comparison between the intensity fluctuations before (I_G illustrated by the blue line) and after (I_G represented by the red line) applying Gaussian smoothing operator. The intensity changes are plotted on the vertical axis when the horizontal axis equals 71. (b) plot on the same horizontal axis when the intensity changes were evaluated on the vertical axis at [222:324] to magnify the observations. According to the figures, it is observable that the intensity fluctuations are dropped, which is evidence that the image is smoother with less noisy pixels. 34

Figure 12: (a) The original image from DRIVE test data (b) Representation of the mask to extract the retina area 35

Figure 13: (a) The output of the Gaussian filtered step followed by masking the undesired border, (b) The enhanced image of ‘a’ using piece-wise matched filtering. 40

Figure 14: Orderly illustration of pre-processing steps: (a) The original fundus RGB image from the DRIVE test data, (b) the extracted green channel, (c) contrast-enhanced image by using the CLAHE algorithm, (d) estimated background using median filter, (e) the blood vessel retention by subtraction of the estimated background from the contrast-enhanced

image, (f) estimated mask of the field of view, (g) Removing the border effect by applying the estimated mask followed by Gaussian filtering, (h) the output of matched filtering step. 41

Figure 15: A mask of 3×3 and the gradient directions 43

Figure 16: Robinson compass kernels. Each mask is sensitive to an edge orientation ranging from 0° to 315° in steps of 45° , where 0° corresponds to a vertical edge, as illustrated in Figure 15. 43

Figure 17: Block diagram of the feature extraction process. “ I_x, I_y, I_z and I_k ” represent the image gradients along the horizontal, vertical, diagonal and anti-diagonal orientations, respectively. 45

Figure 18: Potential vessel edges presented by the image gradients in (a) the horizontal: I_x , (b) vertical: I_y , (c) diagonal: I_z and (d) anti-diagonal: I_k orientations. 46

Figure 19: Fuzzy Membership Functions from MATLAB Fuzzy Logic Toolbox. 51

Figure 20: The components of a Type-1 Fuzzy Inference System [74] 54

Figure 21. Generalized Type-2 Fuzzy Membership Function 55

Figure 22. The footprint of Uncertainty in GT2 FS [54]. 57

Figure 23: The footprint of Uncertainty (Shaded) for IT2FS 58

Figure 24: Architecture of IT2 FIS [75] 59

Figure 25: The membership functions of pixel intensities of four crisp inputs of the proposed IT2 FS, implemented in MATLAB for an image from DRIVE test data. (a) I_x , (b) I_y , (c) I_z , (d) I_k .	62
Figure 26: Proposed IT2 output membership function	63
Figure 27: (a) The original fundus image from the DRIVE dataset, (b) Result of pre-processing, (c) Output of IT2 FS	65
Figure 28: (a) IT2 FS output image, (b) Histogram plot of fuzzy output, (c) Binarized image	67
Figure 29: Comparison of blood vessels images before (a and b) and after (c and d) applying closing operation. (b) and (d) are the magnified copies of (a) and (c), respectively.	70
Figure 30: The result of erosion applied to the binarized image from Figure 29(c)	70
Figure 31: (a) Distribution of connected components, and (b) its magnified plot	71
Figure 32: Visual comparison of the eroded image before (a, b) and after (c, d) CC analysis	72
Figure 33: (a) Original fundus image, (b) Pre-processed image, (c) Output of IT2 FS, (d) Final Segmented Image, (e) Ground truth image	73
Figure 34: Confusion matrix for multi-class machine learning models. The parameters indicate True Positive (TP), False Positive (FP), False Negative (FN) and True Negative (TN)	76

Figure 35: Comparison of the segmentation result by Orujov *et al.* [20] and the proposed method..... 87

Figure 36: Segmentation results from the DRIVE test data 90

Figure 37: Detection of course vessels on an example from DRIVE test data (a) Original Color Image, (b) Magnified optic disk area, (c) Ground truth segmentation, (d) Predicted segmentation 91

List of Appendices

Appendix 1: Methodology MATLAB Code.....	111
--	-----

Abbreviations

1. μm - Micrometer
2. NPDR – Non-Proliferative Diabetic Retinopathy
3. PDR – Proliferative Diabetic Retinopathy
4. ROP – Retinopathy of Prematurity
5. DRIVE – Digital Retinal Image for Vessel Segmentation
6. SVM – Support Vector Machine
7. ANN – Artificial Neural Networks
8. GPU – Graphics processing unit
9. KNN – K-Nearest-Neighbors
10. FCM – Fuzzy C-Means
11. ROI – Region of Interest
12. GWT – Gabor Wavelet Transform
13. RGB – Red, Green, Blue
14. CLAHE – Contrast-Limited Adaptive Histogram Equalization
15. HE – Histogram Equalization
16. 2-D – Two Dimensional
17. FS – Fuzzy System
18. FIS – Fuzzy Inference System
19. IT2 FL – Interval Type-2 Fuzzy Logic

20. GT2 FS – Generalized Type-2 Fuzzy System
21. FOU – Footprint of Uncertainty
22. MF – Membership Function
23. LMF – Lower Membership Function
24. UMF – Upper Membership Function
25. EKM – Enhanced Karnik–Mendel Algorithm
26. CC – Connected Components
27. FOV – Field-of-View
28. TP – True Positive
29. TN – True Negative
30. FP – False Positive
31. FN – False Negative
32. Acc – Accuracy
33. Pre – Precision
34. Se – Sensitivity
35. Sp – Specificity
36. Std – Standard Deviation
37. IoU – Intersection over Union
38. MSE – Mean Square Error
39. PSNR – Peak of Signal to Noise Ratio

Chapter 1: Introduction

1.1. Human Visual System

The visual system is the most important sensory system in humans because it is the brain's largest cortex and contributes to sensing information [59]. The eye catches the light signals by the lens and passes them to sensory cells of the vision system through the retina and are finally interpreted by the visual cortex [60]. The retina is considered the primary tissue of the optical system since it receives the visual information about the coming light and encodes the neural signals to the brain using the photoreceptors in the eye, called cones and rods. Due to the active functionality of the retina, it consumes a large amount of oxygen which subsequently demands an extensive vascular system to keep the retina functioning properly in every circumstance. The retinal blood vessels have a specific thickness range from 50 to 200 μm [59]. The optic disk is where the nerves transfer neural signals from the

retina to the brain. The blood vessels' main branches start from this point and continue through the retina. The smaller vessels tend to meet each other in the macula region. The fovea is the macula part with a pit shape [59].

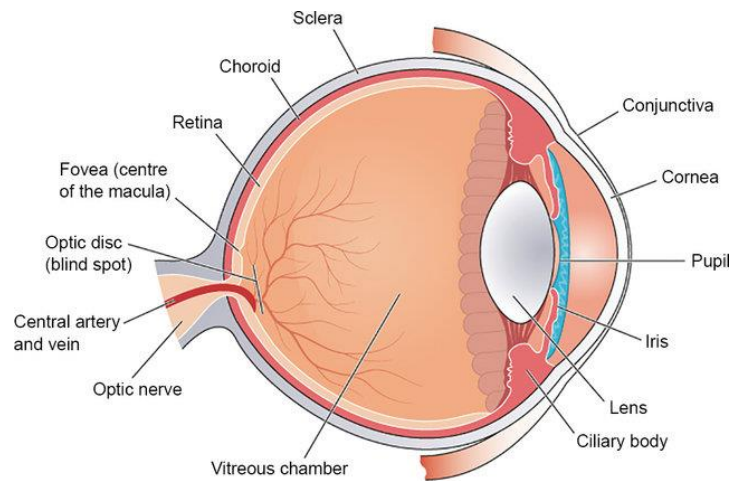


Figure 1: Indication of the human eye structure [61].

Several abnormalities occur in the eyes upon which the structure of the retina and the blood vessels would be subject to change [59]. The medical conditions, including diabetes, hypertension, arteriosclerosis and cardiovascular diseases, can be revealed from inspection of this vasculature system [52]. It has been shown that cardiovascular risk factors, such as blood pressure and body mass index, are related to retinal vessels' morphological features, which play an essential role in coronary heart disease and stroke [40]. The features of blood vessels can be informative given medical diagnosis [41]. For this reason, the primary disorders that affect the retina are overviewed in the next section.

1.2. Retinal Diseases

1.2.1. Diabetes and Diabetic Retinopathy

Diabetes is one of the most health-threatening diseases worldwide by which the body cannot use the produced insulin properly. In other conditions, insulin is not produced by the body. Insulin is a hormone that controls the level of glucose or sugar in the blood. Blood sugar must be carefully regulated so that the body maintains its balance between fats, carbohydrates and proteins. Advanced diabetes can cause damage to organs, including the eyes, kidneys, blood vessels and nerves [62].

Diabetes symptoms can be so mild and hard to diagnose at an early stage. However, early diagnosis of diabetes is critical to let the patients manage the disease and prevent serious complications. The condition of the eye's blood vessels is a factor that is monitored continuously for such patients. Following this fact, the automatic diagnostic methods employing screening over large populations have been admired.

Diabetic Retinopathy (DR) occurs due to damage to the retina's blood vessels in diabetes patients, by which vessels may leak blood and fluid [31, 35, 62]. Such conditions may be moderate or advanced, resulting in sight loss. This issue has become one of the leading causes of vision loss among people aged 25 to 79 years in developing and

developed countries [35]. As an alternative, regular checkups of the retina can diminish the risk of blindness in potential patients [31].

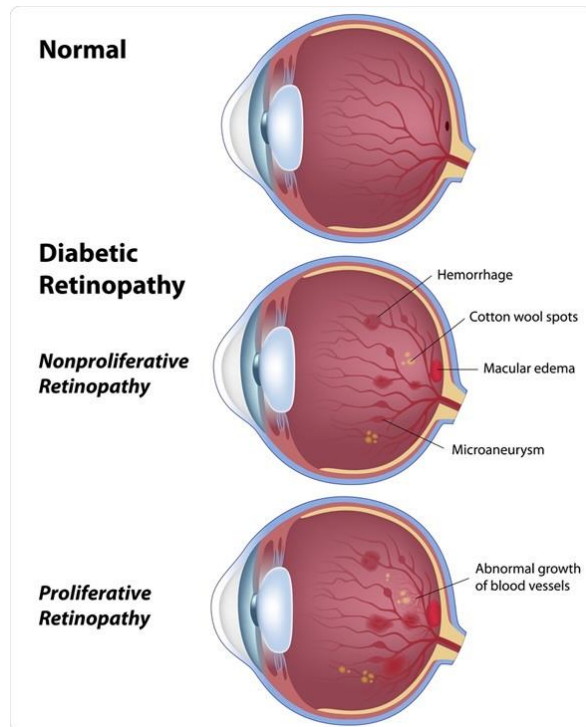


Figure 2: Comparison of retinal blood vessels in regular and DR patients [63].

A fundus camera can monitor retinal abnormalities as a sophisticated non-invasive optical system [36]. At the initial stages of DR, few noticeable symptoms arise from tiny changes in retinal capillaries [62]. DR is categorized into non-proliferative diabetic retinopathy (NPDR) and proliferative diabetic retinopathy (PDR). Microaneurysms are small circular deep-red dots in the fundus. These lumps may open and cause leakage of blood into the retinal tissue [37]. The severity is classified as mild NPDR, whereas macular oedema or hard exudates are moderate NPDR and are recognized by the formation of lipid.

In the advanced phases of retinopathy, the blood vessels are blocked and cause retinal microinfarction (cotton-wool patches) or soft exudates. Finding many such abnormalities results in severe NPDR [62].

PDR is the stage of retinopathy upon which new blood vessels begin to appear within the retina. These new blood vessels are usually abnormal and grow in the centre of the eye. This condition may cause sudden vision loss or permanent blindness [62].

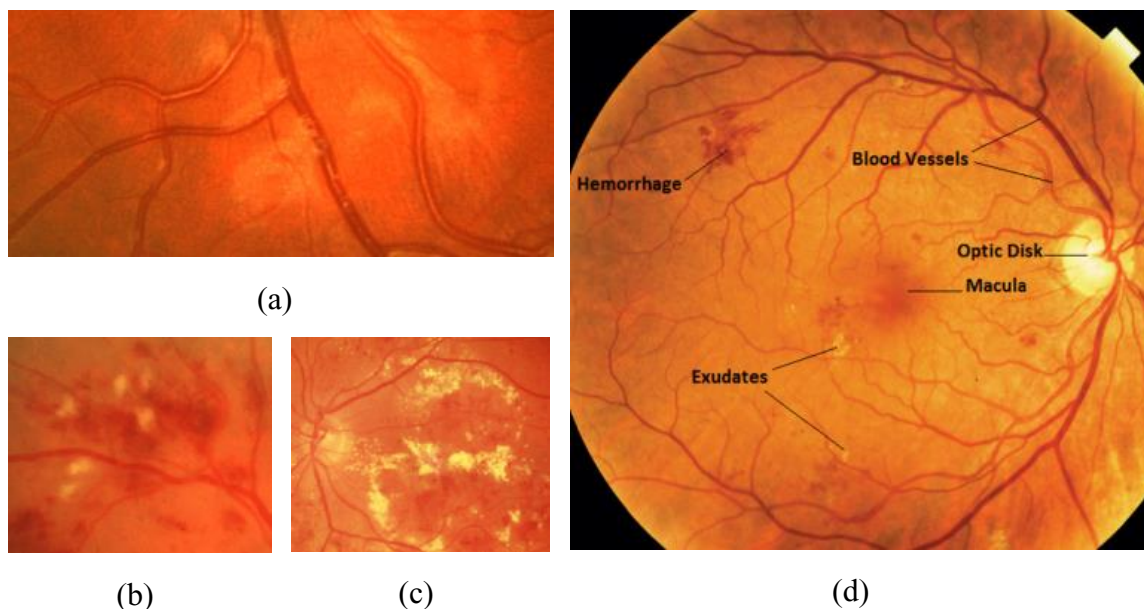


Figure 3: (a) Central vessel reflex and poor contrast, (b) cotton-wool patches, (c) Hard exudates, (d) Retina anatomical structures [64].

1.2.2. Retinopathy Of Prematurity (ROP)

ROP highly impacts childhood blindness while it can be treated by laser surgery in the initial phases of the disease. When the vascular system changes severely in dilation and

tortuosity, a plus disease condition occurs associated with ROP. The state is diagnosed by comparing it to a standard fundus image as the vascular changes can be evidence of disease presence [59].

1.3. Digital Fundus Photography

Over the years, digital fundus imaging has become a common practice for general eye examinations as a non-invasive technique. It facilitates the diagnosis of retina abnormalities, including DR, ROP, arteriosclerosis, and cardiovascular diseases [59]. Since the imaging modality is noninvasive and risk-free, it is beneficial to monitor the patient's state at particular time intervals [59]. Meanwhile, fundus images provide helpful information about the retinal blood vessels regarding diameter and tortuosity.

The system comprises a special microscope with an attached camera by which the eye's interior surface is captured. This surface includes the retina, optic disk, macula and posterior pole. The camera has some modes of color photography, ref-free photography by which the vessel contrast is enhanced, and fluorescence angiography, that illumination of the retina with blue light, can be operated after injecting sodium fluorescein into the blood [64].



Figure 4: Retina examination using Canon digital fundus imaging system [59].

1.4. Motivation

As mentioned, preventing eye difficulties demands regular examinations to monitor the changes in features of blood vessels. The current standard method is applied by ophthalmologists who diagnose many patients. This time-taking procedure may result in diagnosis errors depending on the observer and experience [35,38]. Furthermore, since the vascular system in the retina is complex and the number of vessels is large, manual delineation is a slow and intolerable practice. As a result, computer-aided diagnosis to analyze the retinal images, which takes advantage of image processing techniques, would reduce the workload remarkably [59]. Automatic algorithms can be developed by helping medical experts analyze the images to discover the signs of PDR, NPDR and other conditions.

The first step toward developing such a computer-supported diagnostic system for ophthalmic disorders is automatic blood vessel segmentation by which significant changes in vessels' features can be revealed. Having the segmented blood vessels reduces the chance of false detection of lesions. Besides the application of detected vessels in DR, the segmentation of retinal vessels and their characteristics, including length, width, and branching patterns, can be used for the diagnosis, screening, treatment, and evaluation of various cardiovascular diseases, as well [20,31]. Automatic segmentation of retinal vessels and the analysis of their morphology are helpful for the detection of arteriolar narrowing and foveal avascular regions, retinopathy of prematurity evaluation, and investigation of general cardiovascular diseases and hypertension [38].

1.5. Objectives

The prime objective of this work is to develop a novel and fully automatic approach for localizing retinal blood vessels from digital fundus images. This new method is based on the higher-order fuzzy logic technique, namely, the Interval Type-2 Fuzzy System (IT2 FS), which is more adaptive to new medical data and addresses the uncertainties about the membership functions. Although it is expected to obtain a more favorable result by employing the higher order of fuzzy logic systems, according to the available data, only one experiment has utilized this technique for retinal blood vessel segmentation [20]. The current study contributed a new IT2 FS with newly proposed fuzzy rules that provide

higher performance as a novel approach. Simultaneously, the fuzzy membership functions are adapted to the input image by formulating the membership functions' parameters. The imposed variables of membership functions adjust the uncertainties based on each image and related features. Hence, the algorithm would be more robust to unseen data. Besides, to maximize the contrast of the delivered image to the fuzzy system, the matched filtering technique is applied as a pre-processing step that lets the algorithm better predict the pixels of the retina blood vessels.

The method is desired to be fast, accurate, and practical by untrained community health workers. The algorithm can be employed during the examination of the patient or as a pre-screening method when there is a large volume of data.

1.6. Thesis Formation

The rest of this thesis report is organized as follows. Chapter 2 presents the literature review on previous related works. The chapter divides the complementary approaches into rule-based and supervised methods, of which the benefits and shortcomings are explained.

Chapter 3 discusses the proposed methodology, including the simulation of the main steps of the approach. Also, the basics of fuzzy logic and, subsequently, the mathematical expressions are described in this chapter.

Chapter 4 provides the details regarding the database and the simulation results of the proposed algorithm. An explanation of performance measures is also provided to compare the results with the references from the database. Meanwhile, the performance results of the state-of-the-art algorithms are provided in said chapter.

Chapter 5 discusses the results of the proposed method and evaluates them by comparing them with the related works. The strength and weaknesses of the methodology and possible future works are provided in the same chapter.

Chapter 6 concludes and discusses the thesis in short by talking about the procedure and novelty.

Chapter 2: Literature Review

This chapter reviews and categorizes the recently introduced blood vessel segmentation methodologies in two-dimensional retinal images acquired from the fundus imaging system and tested mutually on Digital Retinal Image for Vessel Segmentation (DRIVE) data set. The chapter aims to describe the algorithms and briefly highlight the performance measures.

Over the years, several researchers have been working on extracting retinal blood vessels. These methods can be divided into two groups: unsupervised and supervised methods. Unsupervised methods apply different image processing filters, mathematical morphology and vessel tracking methods to extract blood vessels [20, 26,31, 38,45, 47, 48, 53,57,65,68]. On the other hand, the supervised methods apply pixel classification techniques to categorize objects in the image as vessels and non-vessels [41, 43, 49, 50,

51, 52]. This chapter has covered and reviewed the most recent works from both perspectives.

2.1. Supervised Methods

Supervised methods are based on training data consisting of the manually labelled images, which help the algorithm learn the rule of vessel extraction defined by the methodology. The manually labelled data are segmented by experts and are considered the gold standard. The methods that use K-nearest neighbor classifier (KNN) [41], Neural Network (NN) approaches [49, 50, 51], or other learning algorithms such as Support Vector Machine (SVM) [43] apply their method to training data and evaluate the result on test data.

Artificial Neural Networks (ANN) apply mathematical weights to determine the probability of belonging to individual output. This procedure is accomplished by training the network with labelled data in an iteration until the error gets below a specific error [64]. Liskowski, Pawel *et al.* [50], trained a deep neural network on a large sample of data after some pre-processing enhancements, and then a network classifies the pixels of the image. The accuracy of classification was 95.66% on the DRIVE database. However, the method depends on feature extraction followed by classification. Indeed, the training level demands accessibility to GPU to perform classification in 8 hours.

The supervised algorithms based on pattern recognition and machine learning mainly detect or classify blood vessel features. Staal, J. *et al.* [41] presented a KNN classifier by extracting image ridges, which coincide approximately with vessel centerlines as the feature vectors. The ridge pixels are grouped in the sets that approximate line elements. Then each image pixel is assigned to the closest line element. The result of the method on DRIVE test data reveals accuracy of 94.41%. The model has some imperfections that reduce the performance of the classification task. Firstly, the algorithm gives a high probability of vessel presence in the boundaries of FOV where no blood vessel exists. The authors introduce this issue as an artifact caused by blurring the images. Secondly, the procedure suffers from false vessel detection in the optic disk region. Thirdly, the method failed to have a good performance on pathological cases. Besides, the segmentation task requires about 15 minutes for an image, making the model improper for real-time treatments.

Soares *et al.* [52] used a Bayesian classifier with the feature vectors that are pixel's intensity and two-dimensional Gabor wavelet transform responses taken at multiple scales to classify each pixel as vessel or background. Their approach achieved an average accuracy of 94.66% on the DRIVE database. However, the algorithm ignores the features relating to the structure and the shape. Also, the authors mentioned a particular dependency of the method on the training data set. A false vessel prediction happened in some images with pathologies and the optic disk area.

SVM as a tool for data classification has been proposed by Ricci *et al.* [43], and they reported 95.95% of accuracy on the same database. At the same time, they evaluated the average grey level along the lines of fixed length passing through the target pixel at different orientations. This feature vector was used for classification with the SVM method. The proposed approach needed fewer features than other supervised techniques that could be extracted more simpler. Also, less data was required for training. However, segmentation of the vessels in the coarse regions and pathological images remains challenging. According to Marin *et al.* [66] experiments, the method suggested by Ricci *et al.* is sensitive to the training set, and it cannot reach the same performance on the unseen data. Hence, the model requires retraining in confronting a new data set.

Marin *et al.* [66] introduced a new supervised method based on Neural Network (NN) to classify pixels in retinal images. The network finds the 7-D vector of grey-level and moment invariant-based features. The preprocessing involves enhancing the contrast of the vessel's borders by opening the operator and removing the background variations using a large mean filter, followed by vessel enhancement. The pixel classification is accomplished by a feed-forward neural network with seven neurons in the input layer, three hidden layers with fifteen neurons each and a single neuron output. The processing time for an image is about 1.5 minutes. The algorithm reached an accuracy of 94.52%, with a robust result on any condition.

The combination of several machine learning techniques for vessel segmentation is proposed by Fraz *et al.* [49], who presented bagging and boosting decision trees and used the orientation of gradient vectors, morphological transformation, line strength measures and Gabor filter response feature vectors. Testing the data on the DRIVE database resulted in an average accuracy of 94.80%. However, the model segments a single image in about 100 seconds.

The main issue with supervised methods is their dependency on robust feature extraction to classify the pixels of the image into vessels and background. Since this feature vector must be calculated for each pixel, the algorithms become almost complicated, and the procedure will be time-consuming due to the training stage [47, 48, 68].

The other point that must be considered is an impactful disagreement between ophthalmologists in identifying vessels [64]. This issue will affect the classification criteria in supervised methods as they depend highly on the gold standard images, which may not be available in real life. Indeed, since the design of the supervised algorithms is based on the pre-classified data, usually, the performance is better than unsupervised algorithms [64]. Besides, training of a supervised algorithm demands the availability of a large dataset to avoid overtraining, which finally results in performance loss when applied to a new database [31].

2.2. Unsupervised Rule-Based Methods

The unsupervised methods do not directly apply ground truth images to the algorithm while they must be present to validate the performance. Usually, these algorithms look for specific patterns of blood vessels in digital fundus images to identify the pixels that belong to vessels.

The vessel centerline extraction method starts from an initial point located manually or automatically. Gagnon *et al.* [39] proposed a vessel tracking method by looking into the border of the optic disk and the boundaries' connectivity after using a canny edge detector. The shortcoming of the module is its dependency on the prior knowledge of the target eye (left/right) and where the image is centred (optic disk or macula). This information requires detecting the optic disk to initialize vessel tracking.

Mathematical morphology is the processing tool for extracting helpful image components that describe region structures such as boundaries. Different morphological operators apply structuring elements to a digital image. Top-hat and watershed transformation operators are commonly used for image segmentation [64]. The advantage of these processing operators is speed and their robustness to noise. Robert Kromer *et al.* [38] used a rules-based method for localizing retinal blood vessels using blood vessel enhancement (morphological opening operation, Gaussian filter, morphological Top-Hat transformation) followed by image binarization. Finally, they tested the result on DRIVE

fundus images and obtained 93.34% accuracy. According to the presented outcomes and the sensitivity of 67.45%, the method performs poorly in detecting the thinner blood vessels and the images suffered from noisy components.

Zana *et al.* [53] made an algorithm based on morphological operators combined with cross-curvature evaluation to segment the vessels. Mathematical morphology extracts the vessels by assuming them to be linear, connected components with smooth curvatures, and cross-curvature evaluation identifies the structures whose curvature is linearly coherent. Niemeijer *et al.* [76] provided a review of some vessel segmentation algorithms. According to the authors' implementations, Zana *et al.* [53] failed to introduce fine vessels while the accuracy was 93.77%.

The opening morphological operation and subtracting the result from the enhanced image have also been used by R. Afrin *et al.* [35] to detect the gray-scale image, which used the single thresholding method to get the binary outcome. Although the model used the basics of image processing, the simple global thresholding led to the loss of many structures of the blood vessels.

Bankhead *et al.* [68] tried to find a fast method for quantifying changes in retinal blood vessels. In the first stage of the algorithm, they used wavelet coefficients for thresholding the fundus images. According to the method, the wavelet coefficients generated at each iteration are wavelet levels whose higher values indicate more extensive features or vessels. Adding these levels results in higher contrast while thresholding the

image based on the highest or lowest level can detect the blood vessels. This approach gained an accuracy of 93.71% on the DRIVE test set.

Fuzzy image processing is a practical mathematical framework and is a collection of all approaches that process the images, their segments and features as fuzzy sets. Since image processing has different aspects of uncertainty, fuzzy logic can be a powerful tool that deals with these uncertainties to manage imperfections [12]. In [31], a method has been proposed using type-1 fuzzy logic and eight feature vectors for each pixel means and medians of intensity values and the first and second nearest neighbor in four directions. Finally, the fuzzy output turns to a crisp gray-scale image binarized by the thresholding method. The average accuracy was 93.82% on DRIVE test data. The run-time of the process was about 3 minutes. Indeed, the technique missed thin vessels with low contrast.

Another algorithm based on fuzzy morphological techniques was introduced in [26] that follows the fuzzy black top-hat transform. The images are preprocessed by the CLAHE (Contrast-Limited Adaptive Histogram Equalization) algorithm to reduce noise and are binarized using hysteresis thresholding after fuzzy top-hat filtering. The algorithm is fast enough to be used in real-time applications and reached an accuracy of 93.80 on the same data.

In terms of fuzzy edge detection, many scientists applied the four direction gradients as the main features of the fuzzy model. Orujov F. *et al.* [20] developed the algorithm that uses CLAHE contrast enhancement and background exclusion on the green

channel of color images. Subsequently, they took the maximum gradient in each pair of mirrored directions and prepared a model based on type-2 fuzzy logic. The membership functions were defined as triangle shapes with straight lines. The image output is binarized after erosion refinements. This method gave an accuracy of 93.9% on DRIVE test data. Although the technique had a high sensitivity of 83.8%, the segmented vessels were remarkably thick in diameter, which led the method to fail in predicting the lesions and pathologies. This issue was reflected in the Jaccard value of only 38%, indicating the poor similarity between the segmented image and the ground truth.

Tolias Y. *et al.* [67] developed an algorithm based on fuzzy C-mean (FCM) clustering that describes each pixel as a vessel or non-vessel. Firstly, the optic disk is detected to specify the starting point, and then it uses the fuzzy vessel intensity information to track the vessels in segmented regions. The algorithm was evaluated using a manually segmented image, and they concluded that the overall performance was good enough to follow the blood vessels.

FCM clustering has also been used by K. Khatter *et al.* [57]. At first, the fundus images were preprocessed by either the CLAHE method or the combined response of the Gaussian kernel and Gabor filter. The Robinson Compass Mask was applied to extract eight orientations concerning different directions in the feature extraction stage. A fuzzy C-means model was then used to accomplish segmentation. Depending on the pre-processing methodology, the report had two accuracy values. The CLAHE method reached

92.62% accuracy for 20 DRIVE test samples, while the second pre-processing method obtained 93.71% on the same database. Based on the represented segmented image by the authors, the technique had a poor performance on optic disk area and detecting the thinner vessels.

Matched filtering is another technique that is commonly used in image segmentation applications. The method was used by Chaudhuri S. *et al.* [46] with a linear kernel with a Gaussian profile to segment retinal images, which matched with a Gaussian or Gaussian derivative curve shape of blood vessels. The kernel was rotated every 15° to cover blood vessels with different orientations. Then the highest response was selected for each pixel. This image was binarized by the global method of Otsu thresholding that misses small objects such as thin vessels and branches. An estimation of the result of this algorithm on DRIVE test data was provided in [47], with an average accuracy of 87.73%. Such low accuracy can be caused by the global method of binarization and the lack of proper preprocessing strategies.

The Gabor wavelet seems to provide valuable results in retinal image analysis. Kumar, Kundan, *et al.* [47] applied top-hat filtering on the green channel of the RGB image from DRIVE data and enhanced the vessels' contrast by the CLAHE algorithm. 2-D Gabor transform filter was applied to this preprocessed image, and the binarized image was obtained by Otsu's method as a global thresholding approach. This process had an accuracy of 94.32%.

Da Rocha *et al.* [48] performed pre-processing on the green channel of the RGB images from the DRIVE database by creating the complement of the image and making a mask of the region of interest (ROI) of the retina area, followed by an adaptive method of histogram equalization. The next step consists of 2D Gabor Wavelet Transform (GWT) and closing operation. This procedure obtained an average accuracy of 94.62%. The method showed limited performance in pathological images.

Al Shehhi, Rasha, *et al.* [65] proposed an algorithm that followed three main steps: filtering-based correction to remove noise in the background, a morphological-illumination enhancement to detect blood vessel edges and hierarchical graph-based segmentation that applied some concepts such as similarity and closure of spectral or spatial features between nodes in graphical multilayers. Although the algorithm reached the accuracy of 93.4% on the DRIVE test set, the extended run-time was an issue in real-time applications.

Chapter 3: Methodology

In the following chapter, the proposed method is explained while it consists of four main steps: (1) pre-processing, (2) feature extraction, (3) fuzzy logic algorithm, and (4) post-processing. A flowchart of the algorithm is shown in Figure 5. Each stage includes some processing levels.

The main body of the algorithm is based on the concept of an interval type-2 fuzzy system; however, to minimize the effect of noise on the fuzzy algorithm parameters, different pre-processing steps are employed. The leading rule of pre-processing is to turn the digital color image of the input to grayscale and enhance the image so that the contrast between the vessels and the background reaches the highest possible level.

In the second stage, the feature extraction algorithm aims to find some specific patterns in the image to feed them into the fuzzy logic algorithm, where fuzzy sets and rules are created to evaluate the extracted features and detect the potential vessel edges.

The input and output membership functions' parameters are no longer strictly defined in the proposed methodology. In contrast, the input image is evaluated. Their intensities are utilized to form the bell-shaped membership functions according to the input gray levels, so each of the four fuzzy inputs has individual membership functions. This approach is expected to have a better result as it adapts to the relating input.

In the final stage, the algorithm binarizes the grayscale image, and the quality of detected blood vessels improves by shrinking the identified vessel area and removing noise.

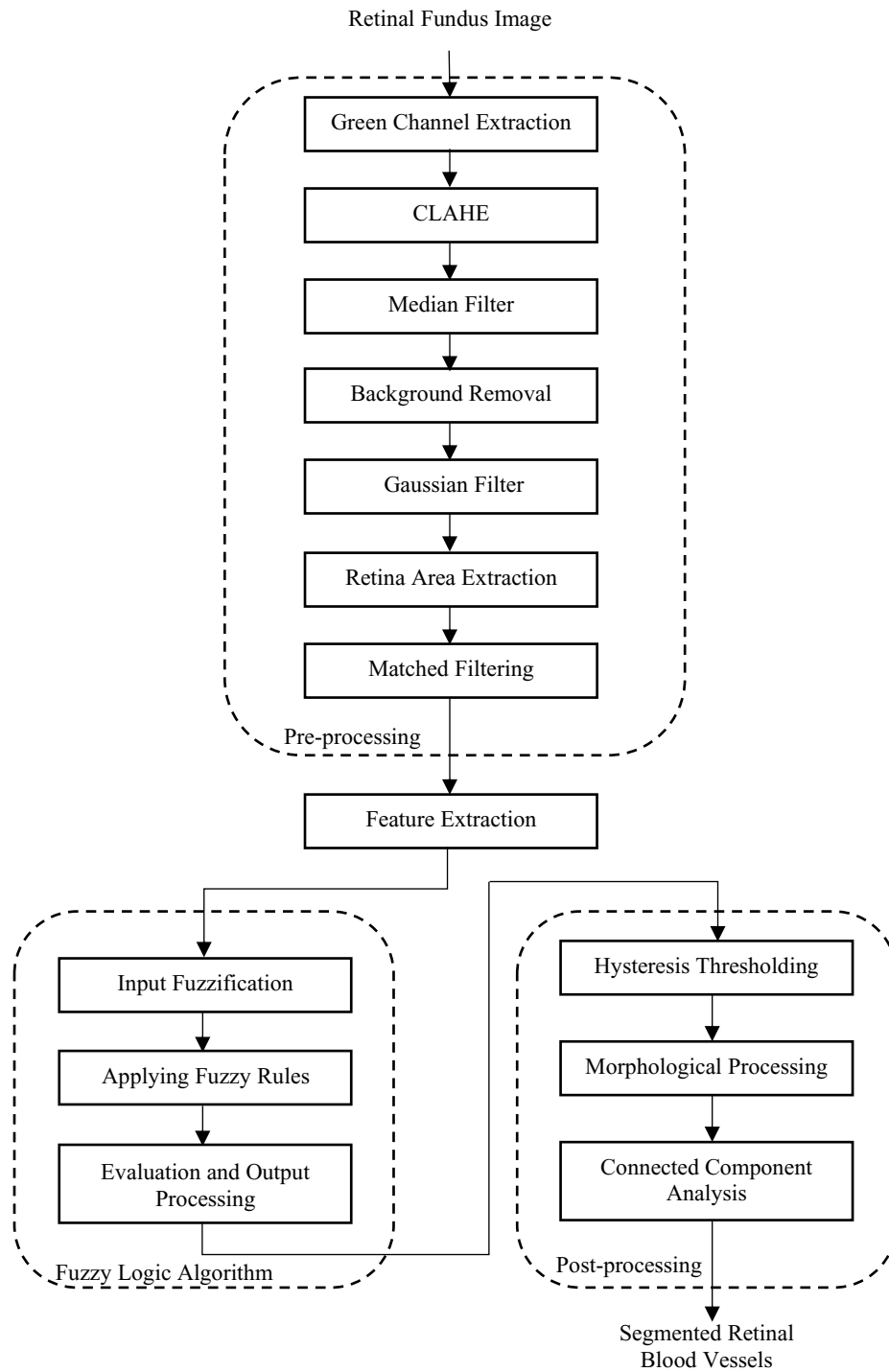


Figure 5: A flowchart of the proposed method

3.1. Pre-processing

Retinal images suffer from poor contrast and noisy background like any image taken from various medical imaging modalities. For this reason, pre-processing is a crucial stage in image segmentation algorithms that directly impacts the output performance.

In this research, a compact algorithm is developed that follows specific steps to reach an enhanced copy of the initial fundus image while the vessels are more visualized. In the following section, the pre-processing stages are explained separately.

3.1.1. Green Channel Extraction

The system's input is an RGB image consisting of three different channels, each of which represents the color value of the pixels. Because the blood vessels have dark color in a specific intensity range, it is expected that they belong to a particular channel that represents their value better than the others. In the first pre-processing steps, it is necessary to extract this color channel of the image with the highest contrast between blood vessels and the background. Comparing the three channels; presented in Figure 6, one can confirm that the green channel has the most details of retinal blood vessels while the red channel suffers from bright pixels, and the blue channel is poor in dynamic range.

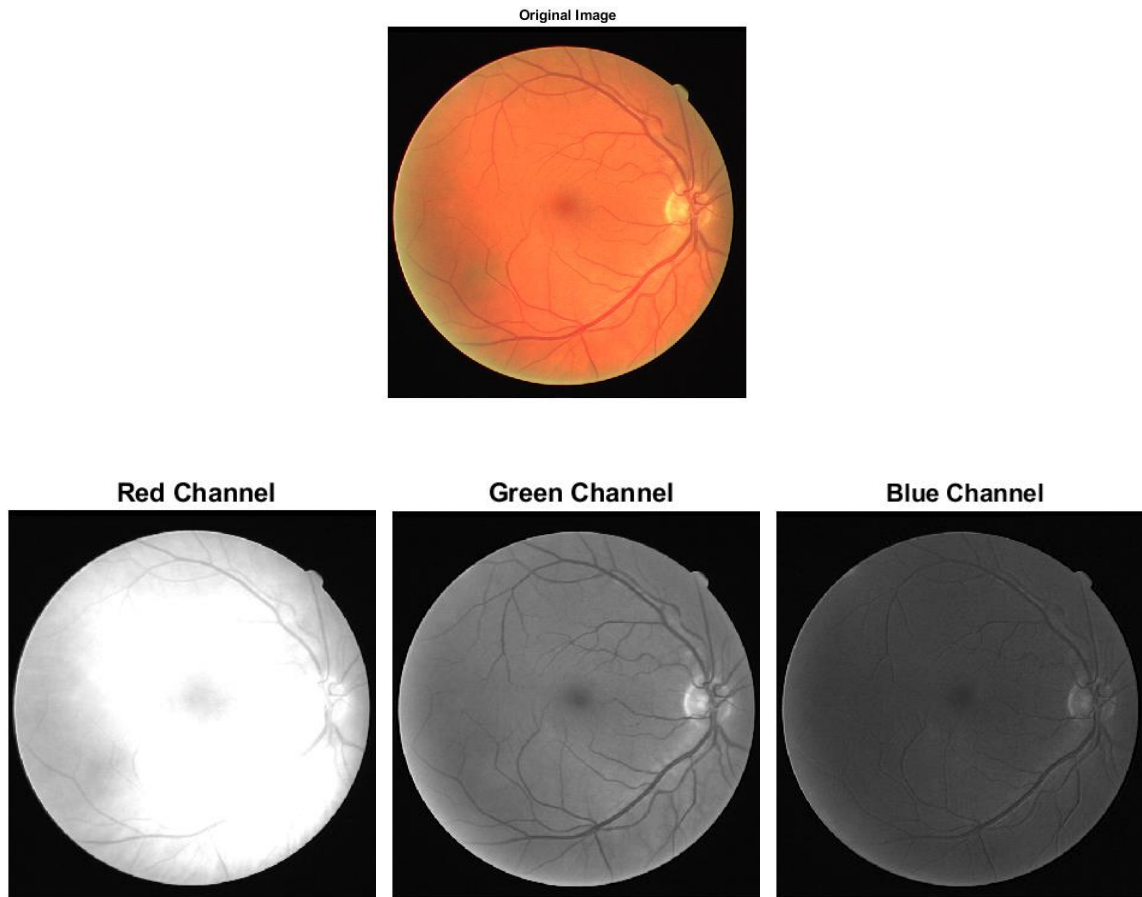


Figure 6: Visualization of a color digital fundus image and individual RGB channels from the DRIVE dataset

From the other point of view, the three-channel RGB images can directly turn into a gray-level image where a value replaces the information carried by each pixel in the range of $[0 \ 255]$ in 8-bit positive integers. A simple comparison between the extracted green channel and the grayscale image confirms that due to a higher contrast of the blood vessels, the green channel of the RGB image is a better candidate for further processing.

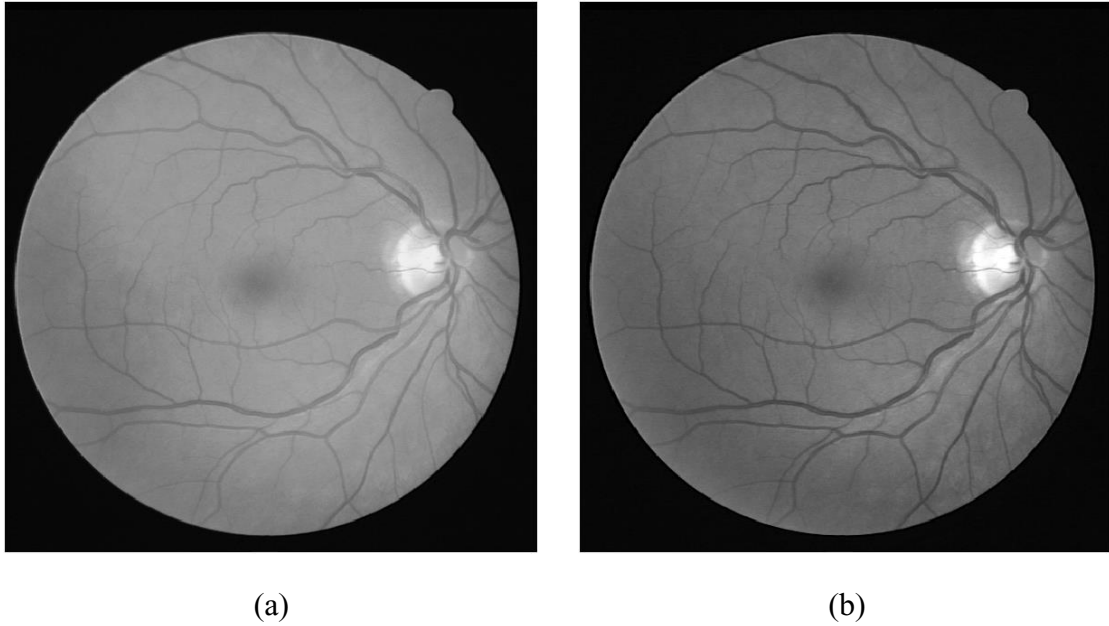


Figure 7: Illustration of (a) the grayscale image and (b) the green channel of an RGB image from the DRIVE dataset

3.1.2. Contrast-Limited Adaptive Histogram Equalization (CLAHE)

As a pre-processing step to increase the contrast between the background and blood vessels, histogram equalization is a popular technique that creates a uniform distribution among the image intensities by stretching the histogram and extending the frequencies in an image. A standard histogram equalization enhances the global contrast of the image [Figure 8(c)]. However, the advanced form of histogram equalization computes histograms on smaller regions and enhances local contrast. The CLAHE algorithm is an adaptive histogram equalization that remaps the grayscale values of the image on each of the smaller areas [45]. This technique is widely used in medical image processing [48].

In the method of CLAHE, the image is divided into regions called tiles, while histogram equalization is applied on each tile individually. Different types of distribution functions can be assigned to the shape of the histogram and are used for creating the contrast transform function for each tile. So, the contrast of each tile improves independently. Then, the tiles are merged with neighboring regions using bilinear interpolation to avoid the blocking effect [21].

In practice, a tile covering a homogenous neighborhood (background) will take a high peak in the histogram of that tile. The clip limit is a factor that prevents noise amplification in uniform regions by accumulating histogram bin values higher than the clip limit and distributing them into other bins. This process helps to reduce enhancement in such areas [26]. If the clip limit were not applied, the transformation function in histogram equalization would be a cumulative histogram. Figure 8 compares using both histogram equalization techniques (HE) and CLAHE on the green channel of a fundus image from the DRIVE database. According to these images and their histogram, it is noticeable that the standard histogram equalization spreads out the intensities throughout the image while it saturates to the brightest values in some parts relating to the non-vessel regions. Such stretched histogram addresses this issue by including a wide range of intensities through the bright values. Contrarily, the CLAHE algorithm was capable of increasing the contrast between the background and the blood vessels with less contribution to amplifying the noise.

After examining several functions, a bell-shaped Rayleigh distribution was selected due to its power to provide the best contrast. The tiles' size and other parameters have been chosen by trial and error and evaluation of the final segmented image in terms of accuracy and sensitivity. So, the image was divided into tiles of 9-by-9, and the clip limit value was set to 0.02.

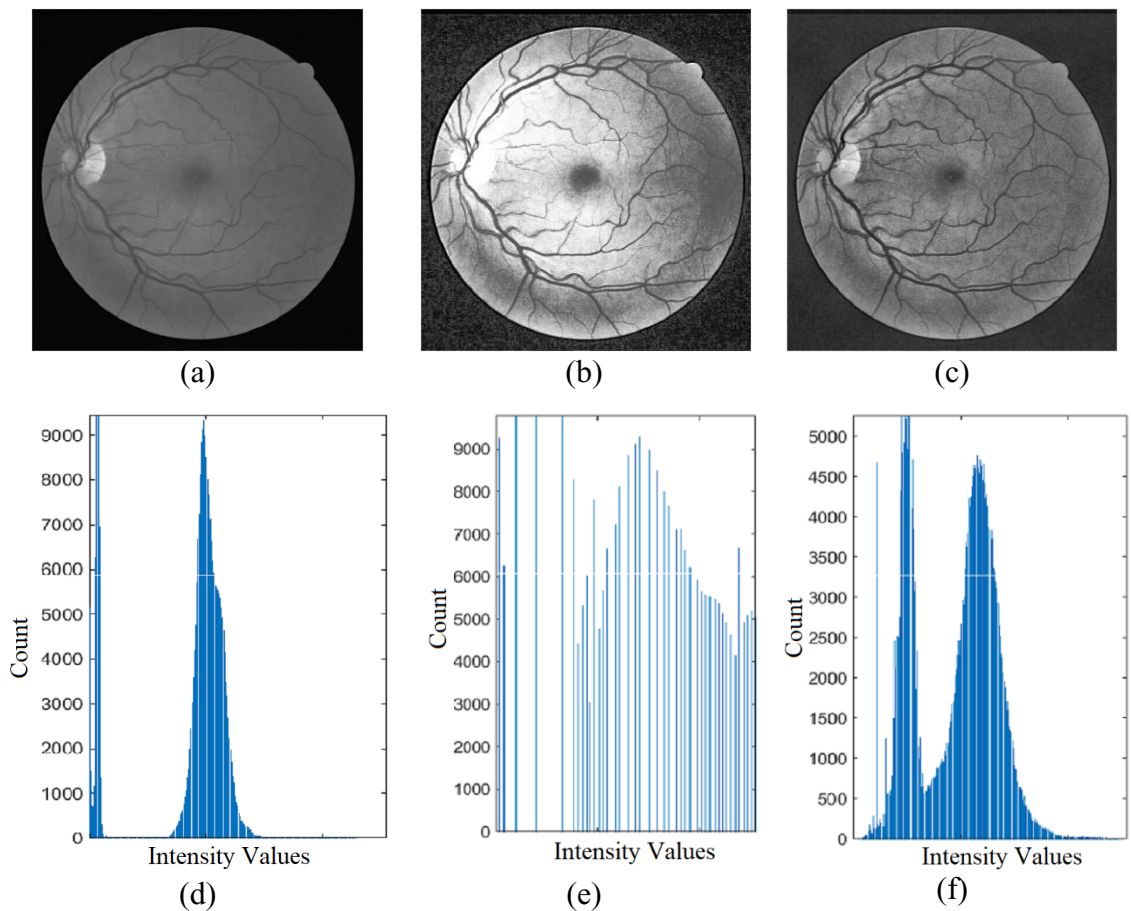


Figure 8: Comparison of standard histogram equalization (HE) and Contrast-Limited Adaptive Histogram Equalization (CLAHE). Top row: (a) Green channel of an image from DRIVE test data, (b) Enhanced image using HE processing, (c) Contrast-improved image using CLAHE processing. Bottom row: The histograms of the corresponding images (a,b,c) are visualized. Results show that applying the CLAHE method makes the blood vessels more apparent while the noise is less amplified.

3.1.3. Median Filter and Background Removal

By carefully examining the derived image from CLAHE processing, it can be noticed that the thinner blood vessels cannot be distinguished easily. Therefore, there is a requirement to design a strategy that tackles this issue. The idea was to exploit the complement of the image and remove the background fluctuations. This technique is also beneficial in recognizing the extra noise more straightforwardly.

Estimating the background is the task that can be done using a low pass filter that smooths out the image and blurs it. In this work, two low-pass filters have been applied to the image to discover the best result that keeps the blood vessels in bright pixels.

The median filter replaces each central pixel value in a kernel with the median of neighboring pixel values [2, 20]. The procedure is accomplished by sorting the pixel values in a window into numerical order and then considering the middle pixel value. By this definition, a median filter with a large kernel of 45×45 creates a blurred image and reduces the overall variability in each window by choosing the mid-positional value. Since this value is more probable to belong to the background, this filter size can be accounted for as a background estimation. Hence, this filtration is applied to the image, and the result is stored in a matrix called $I_{med}(x, y)$.

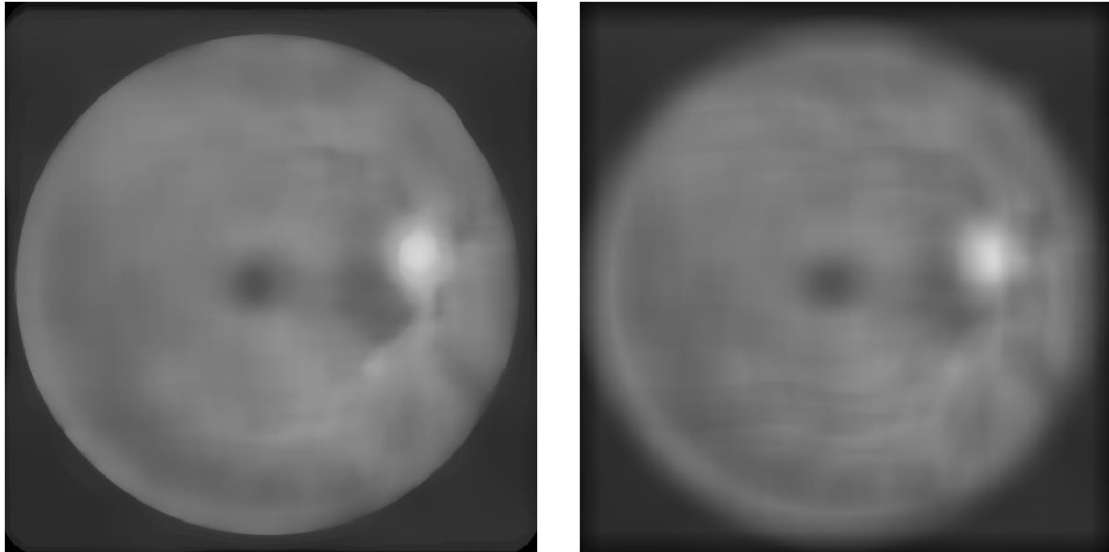
$$I_{med}(x, y) = Med_{(i,j) \in w} [I_e(i, j)] \quad (3.1)$$

In this expression, the kernel is demonstrated by w with the pixel center of (x, y) . I_e is the contrast-enhanced image obtained from the CLAHE method, and $Med_{(i,j)}$ is the median in each kernel that is replaced by the corresponding pixel value in the position of (i, j) in I_e .

Following this procedure, the background is eliminated (I_s) by subtracting the median filtered image from the contrast-enhanced image from the previous step.

$$I_s = I_{med} - I_e \quad (3.2)$$

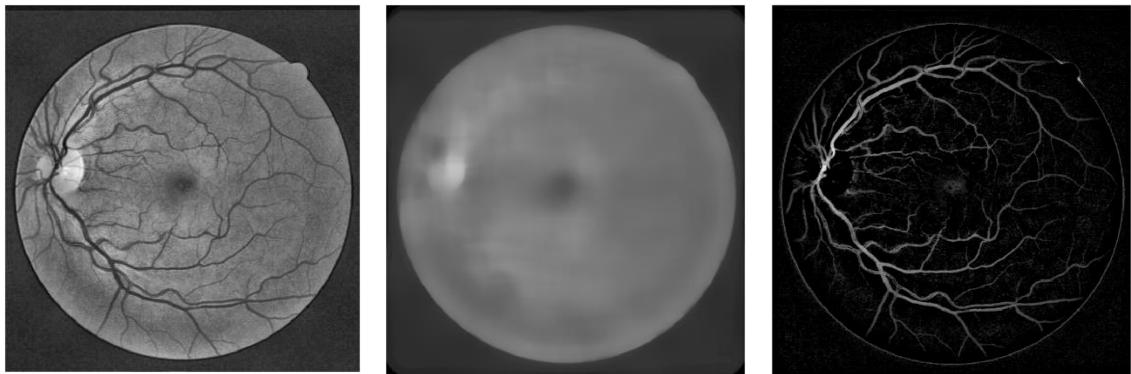
Another choice of filter is a moving-average filter with the said kernel size. Figure 9 compares the estimated background from both averaging and median filters. According to the results, the median filter keeps more edges and structures of the image, meaning that the effect of blurring would be less sensible using the non-linear median filter. On the other hand, after applying the subtraction operation, the moving average filter leaves a shadow on the blood vessels that brings fewer pixels of the vessels to the bright side. Consequently, the median filter has been chosen to attain the mentioned goal of this processing step. Figure 10 represents the background removal procedure from which I_s mainly contains the vessels and the circle of the retina region while the optic disk area has been removed.



(a)

(b)

Figure 9: Estimated background using (a) median filter and (b) moving-average filter. Results show the moving-average filter shades of blood vessels through the estimated image.



(a)

(b)

(c)

Figure 10: Background exclusion process. (a) Contrast-enhanced image by CLAHE, (b) Median filtered image, (c) Subtraction of 'b' from 'a'

3.1.4. Gaussian Filtering

Gaussian filter is a spatial filter to smooth the image and remove the noise. This operator uses a Gaussian or bell-shaped kernel with the equation below [12]:

$$G(x, y) = \frac{1}{2\pi\sigma^2} e^{-\frac{x^2+y^2}{2\sigma^2}} \quad (3.3)$$

Based on this operator, the standard deviation value (σ) is taken from the under-processing image with the kernel size of 3. Also, x and y are the distances from the origin on the horizontal and vertical axes, respectively. Finally, the filter convolves with I_s , as the background-removed image from the previous step and creates the so-called I_G .

By experiencing different filter methods, it has been concluded that this step of smoothing will result in higher accuracy because it removes more small noisy dots from the background and makes it less fluctuated. At the same time, it keeps the boundaries of the blood vessels. A specific line of the image from I_s and I_G is compared to evaluate the effect of this filtering step. Figure 11(a) represents the intensity changes in the vertical axis when the horizontal axis is constant and is equal to 71. Figure 11(b) is plotted on the same horizontal axis when the intensity changes were evaluated on the vertical axis at [222:324] to magnify the observations. According to the Figures, it is observable that the intensity fluctuations are dropped, which is evidence that the image resulted in less noisy pixels.

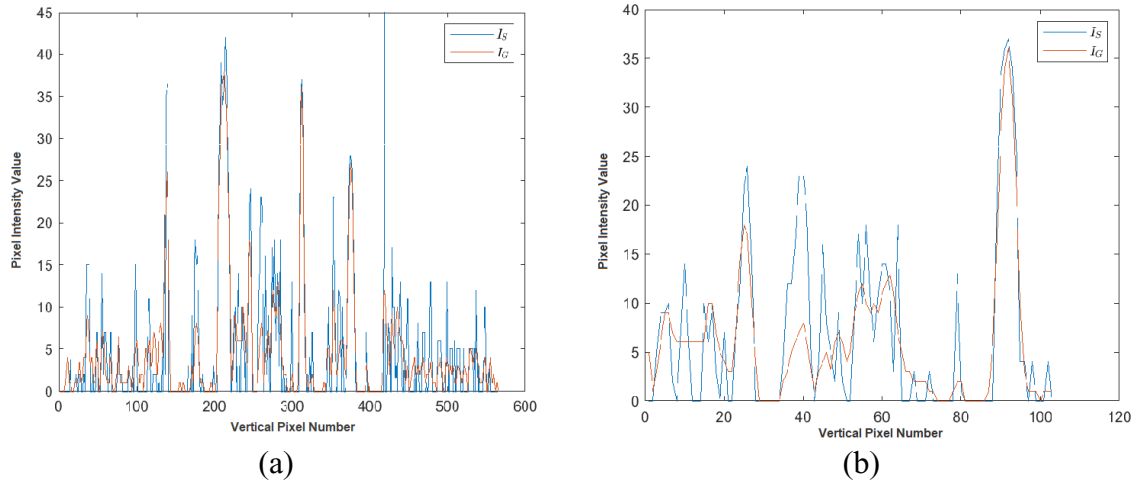


Figure 11: (a) Comparison between the intensity fluctuations before (I_S illustrated by the blue line) and after (I_G represented by the red line) applying Gaussian smoothing operator. The intensity changes are plotted on the vertical axis when the horizontal axis equals 71. (b) plot on the same horizontal axis when the intensity changes were evaluated on the vertical axis at [222:324] to magnify the observations. According to the figures, it is observable that the intensity fluctuations are dropped, which is evidence that the image is smoother with less noisy pixels.

3.1.5. Retina Area Extraction

A bright circle around the retina area is observable on the processed image. This ring has been produced because of having an expected intensity range with the blood vessels. This issue interferes with the edge detection process of the blood vessels and results in false positives. Therefore, this region must be ignored for further processing.

The luminance of the original RGB image was employed to create a mask for the region of interest. It is considered that foreground and background color combinations provide sufficient contrast. The three channels of the original image, denoted by R , G , and

B , are applied to the Luma formula (3.4). This expression is the weighted sum of the components of the color image and represents the image brightness with $L(x, y)$ [26].

$$L(x, y) = 0.2989 \times R(x, y) + 0.5870 \times G(x, y) + 0.1140 \times B(x, y) \quad (3.4)$$

In the next step, the image is scanned to find the foreground border that is assumed to be the start of the retina and assign zero to any pixel which is smaller than the mean value of the L matrix. This approach helps remove the background that will rarely contain the blood vessels [26]. The indication of the mask resulting from this step of pre-processing is presented in Figure 12. In the end, the mask is applied to the output of the preprocessed image to clean up the background fluctuations.

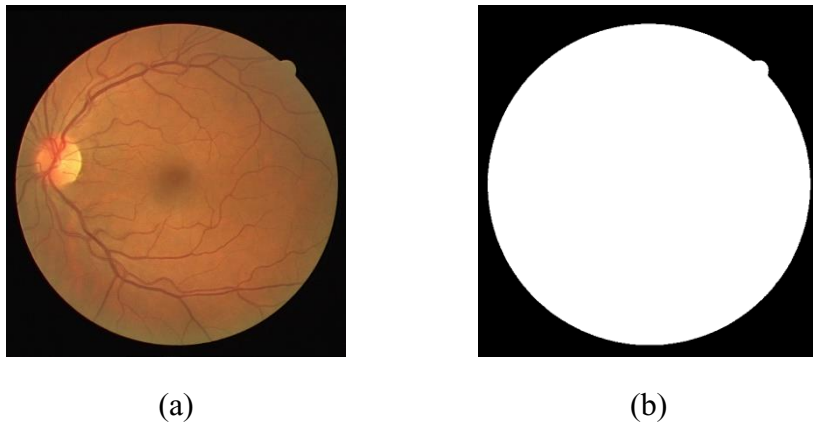


Figure 12: (a) The original image from DRIVE test data (b) Representation of the mask to extract the retina area

3.1.6. Matched Filtering

Matched filters are linear and time-invariant filters widely used to increase the signal-to-noise ratio. A piece-wise linear segment detection technique can be done using a matched filter. This concept was first applied to retinal blood vessels by Chaudhuri, S. *et al.* in 1989 [46]. The retinal image convolves with a template that models the blood vessel's structure according to the proposed method. Consequently, the result represents a higher contrast between the blood vessels and the background. The contrast-enhanced result is convincing to employ such a filter before heading to the next level of the algorithm.

Chaudhuri [46] reported that the blood vessels are assumed to have specific features that are helpful in the design of the filter kernel. Firstly, vessels consist of two edges that are running in parallel. Here, it has been assumed that the vessels do not have many curvatures and accordingly, linear pieces can estimate them. Secondly, looking at the retinal images, one can confirm that the diameter of the vessels decreases as they distance from the optic disk. Chapter one mentions this specific thickness range changes between 50 to 200 μm . However, this changing diameter has been assumed to be a constant for simplicity. Thirdly, although the pixels' intensity changes slightly among the vessels, their cross-section is expected to follow a standard Gaussian distribution. Therefore, it may be approximated by a Gaussian curve for all blood vessels.

According to this article [46], the concept of the matched filter in 2D images is firstly defined on a one-dimensional signal of $s(t)$ with Gaussian noise with the spectrum of $\eta(f)$. Assuming a filter has the transfer function of $H(f)$, the output of the signal can be achieved from the inverse Fourier transform of $S(f)$:

$$s_0(t) = \int H(f)\{S(f) + \eta(f)\} \exp(j2\pi ft) df \quad (3.5)$$

In [72], the authors prove that the optimum signal in the presence of such noise is obtained in the Fourier domain as below:

$$H_{opt}(f) = S^*(f) \quad (3.6)$$

It must be noted that $s(t)$ is a signal with only real values. So, according to Fourier transform properties, $h_{opt}(t) = s(-t)$ is the matched filter for the signal $s(t)$. Regarding the blood vessels, it is assumed that the intensity profile has a Gaussian shape in each line that connects the mirrored edges. This shape is supposed to be symmetrical because its mean value is located in the center of the vessels. Thus, $s(-t) = s(t)$ and as such, $h_{opt}(t)$ takes the same characteristics and can be estimated by a Gaussian function.

This work uses the concept of matched filtering by comparing the cross-sections with identical profiles along their length. Let's say that the blood vessels have a fixed

orientation along the y-axis in a specific line such as l . Following the mentioned assumptions, the vessels are expected to have a normal intensity distribution. Hence, the convolution kernel can be described by a Gaussian shape of (3.7) in the explained 1-dimensional problem [46], where σ is the expansion of the intensity profile. In this case, the blood vessels are characterized by bright pixels. For this reason, the negative sign of the original equation is eliminated.

$$K(x, y) = \exp(-x^2/2\sigma^2) \text{ for } |y| < l/2 \quad (3.7)$$

However, the vessels have different orientations, and thereby the convolution kernel needs to be applied at several rotations meaning that the kernel has to be rotated accordingly. Supposing a discrete point of $\bar{p} = [x, y]$ in the kernel to rotate the point through an angle θ_i that matches the new orientation of the vessel in the i -th kernel; the following matrix has been used [46]:

$$\bar{r}_i = \begin{bmatrix} \cos \theta_i & -\sin \theta_i \\ \sin \theta_i & \cos \theta_i \end{bmatrix} \quad (3.8)$$

The corresponding point in the rotated coordinate will be $\bar{p}_i = [u, v]$, and it is calculated using the equations below [46]:

$$\bar{p}_i = \bar{p} \bar{r}_i^T \quad (3.9)$$

$$u = x \cos \theta_i - y \sin \theta_i \quad (3.10)$$

$$v = x \sin \theta_i + y \cos \theta_i \quad (3.11)$$

According to Chaudhuri S. [46], angular increments of 15° are needed to have 12 different kernels to fit into all possible orientations of vessels. A Gaussian curve has two trails that continue to infinity. These trails are limited to $u = \pm 3\sigma$. So, A neighborhood N is expressed in a way that $N = \{(u, v) \mid |u| < 3\sigma, |v| < l/2\}$ [46]. Accordingly, the weights in the i -th kernel are given by (3.12).

$$K_i(x, y) = \exp(-u^2/2\sigma^2) \forall \bar{P}_i \in N \quad (3.12)$$

Let's say A is the number of points in N . Then, the mean value of the i -th kernel is:

$$m_i = \sum_{\bar{p}_i \in N} K_i(x, y) / A \quad (3.13)$$

Because the background is assumed to have a constant intensity with zero mean value, the convolutional mask used in this filter is given by subtracting the kernel from its mean value by using (3.14).

$$K'_i(x, y) = K_i(x, y) - m_i \forall \bar{P}_i \in N \quad (3.14)$$

At last, a set of 12 kernels are convolved with the so-far pre-processed image, and at each pixel, only the maximum of their responses is kept. In the work of Chaudhuri S. *et al.* [46], this method has been binarized directly to be used as the primary retinal segmentation method. However, it has been shown that the matched filter response can be more effective when combined with other methods [64]. The value of l was determined experimentally after analyzing vessels, and it was set to 7, and the sigma value (σ) was 1.5. This model was selected in the pre-processing stage because it reduces the possibility of false detection of blood vessels in noisy images by sharpening their edges and giving the thin blood vessels more chance to be correctly selected. This efficacy is favorable when the image passes through the fuzzy logic stage. The effect of this filter on increasing the contrast between the blood vessels and the background is observable in Figure 13(b).



Figure 13: (a) The output of the Gaussian filtered step followed by masking the undesired border, (b) The enhanced image of ‘a’ using piece-wise matched filtering.

Figure 14 summarizes the main pre-processing steps using a fundus image from the DRIVE data set.

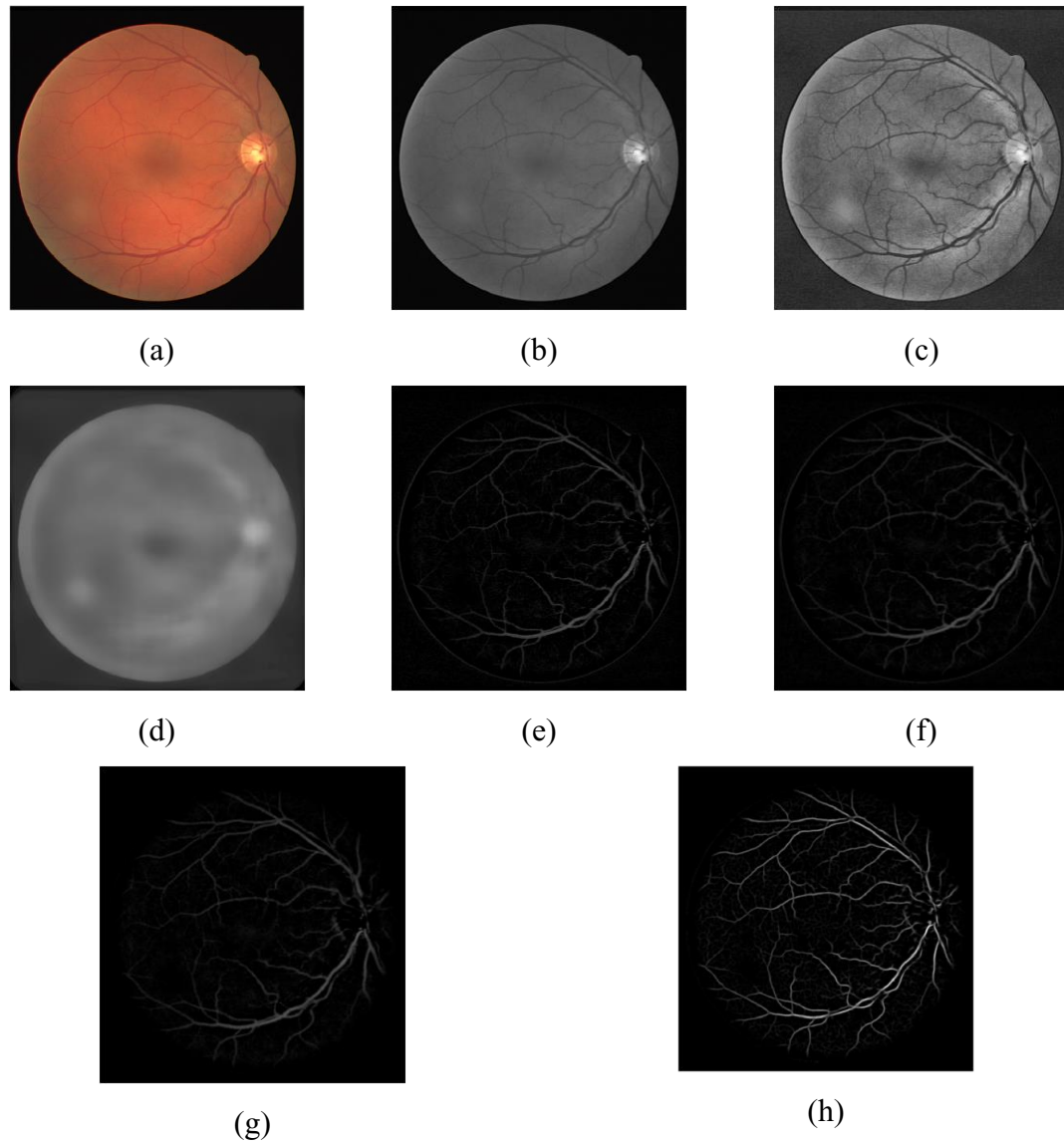


Figure 14: Orderly illustration of pre-processing steps: (a) The original fundus RGB image from the DRIVE test data, (b) the extracted green channel, (c) contrast-enhanced image by using the CLAHE algorithm, (d) estimated background using median filter, (e) the blood vessel retention by subtraction of the estimated background from the contrast-enhanced image, (f) estimated mask of the field of view, (g) Removing the border effect by applying the estimated mask followed by Gaussian filtering, (h) the output of matched filtering step.

3.2. Feature Extraction

The design of a fuzzy logic inference system demands introducing some features of the pre-processed image as the crisp inputs. At this stage, the proposed method is inspired by Orujov F. *et al.*'s article [20] to select the features based on the gradients of the image in a mask of 3×3 . A gradient is the first derivative of an image that expresses the rapid changes in intensity in different orientations [57]. The image gradient is a 2-dimensional vector that points to the direction of the most significant intensity, while its magnitude indicates the rate of change in that direction.

Many researchers have used the horizontal, vertical, diagonal and anti-diagonal gradients of the image as they are good representatives of image edges [10,11,17,18,27,41,48,49,56]. Figure 15 shows eight directions defined on a 3×3 mask, each expressing the intensity changes in the corresponding orientation.

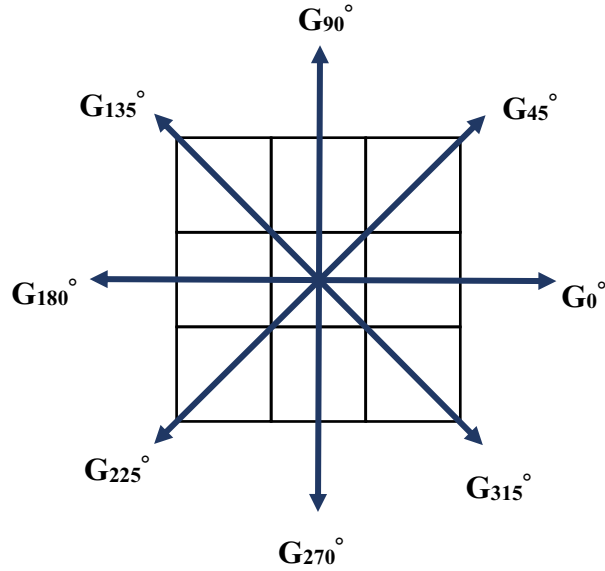


Figure 15: A mask of 3×3 and the gradient directions

The method utilizes Robinson Compass Mask to extract the features from the image. Figure 16 introduces the corresponding kernels resulting from a single mask and rotating it to form eight orientations.

$\begin{bmatrix} -1 & -2 & -1 \\ 0 & 0 & 0 \\ 1 & 2 & 1 \end{bmatrix}$	$\begin{bmatrix} -2 & -1 & 0 \\ -1 & 0 & 1 \\ 0 & 1 & 2 \end{bmatrix}$	$\begin{bmatrix} -1 & 0 & 1 \\ -2 & 0 & 2 \\ -1 & 0 & 1 \end{bmatrix}$	$\begin{bmatrix} 0 & 1 & 2 \\ -1 & 0 & 1 \\ -2 & -1 & 0 \end{bmatrix}$
G_0°	G_{45°	G_{90°	G_{135°
$\begin{bmatrix} 1 & 2 & 1 \\ 0 & 0 & 0 \\ -1 & -2 & -1 \end{bmatrix}$	$\begin{bmatrix} 2 & 1 & 0 \\ 1 & 0 & -1 \\ 0 & -1 & -2 \end{bmatrix}$	$\begin{bmatrix} 1 & 0 & -1 \\ 2 & 0 & -2 \\ 1 & 0 & -1 \end{bmatrix}$	$\begin{bmatrix} 0 & -1 & -2 \\ 1 & 0 & -1 \\ 2 & 1 & 0 \end{bmatrix}$
G_{180°	G_{225°	G_{270°	G_{315°

Figure 16: Robinson compass kernels. Each mask is sensitive to an edge orientation ranging from 0° to 315° in steps of 45°, where 0° corresponds to a vertical edge, as illustrated in Figure 15.

The masks convolve with the image to take the edges in the corresponding orientation directly from the kernel with the maximum response. Assuming the output of pre-processing step is I_p , the image gradients can be found by equation (3.15).

$$g_{degree}(x, y) = G_{degree} * I_p(x, y) \quad (3.15)$$

In the expression above, g is the gradient of the pre-processed image in several *degree* values demonstrated in Figure 15, and it is derived from convolving the corresponding kernel (G_{degree}) with I_p .

As shown in Figure 15, the masks are symmetrical to the vertical, horizontal, diagonal and anti-diagonal axis. Accordingly, the mirrored gradients are combined after comparing them and computing the maximum value for every image point. Finally, the result would be four images that contain the highest response for each pair of mirrored gradients. These four matrices, I_x , I_y , I_z and I_k are used as the features fed into our fuzzy system as the crisp inputs for further processing. The block diagram of feature extraction is mentioned in Figure 17, and the candidate pixels of the retinal image by each feature are visualized in Figure 18.

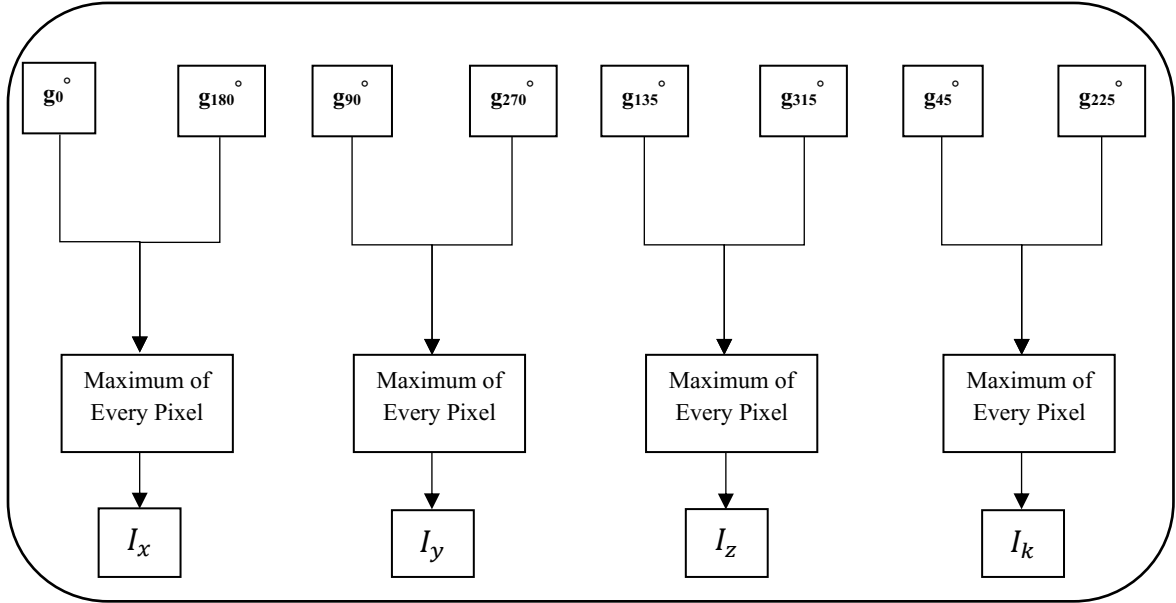


Figure 17: Block diagram of the feature extraction process. “ I_x, I_y, I_z and I_k ” represent the image gradients along the horizontal, vertical, diagonal and anti-diagonal orientations, respectively.

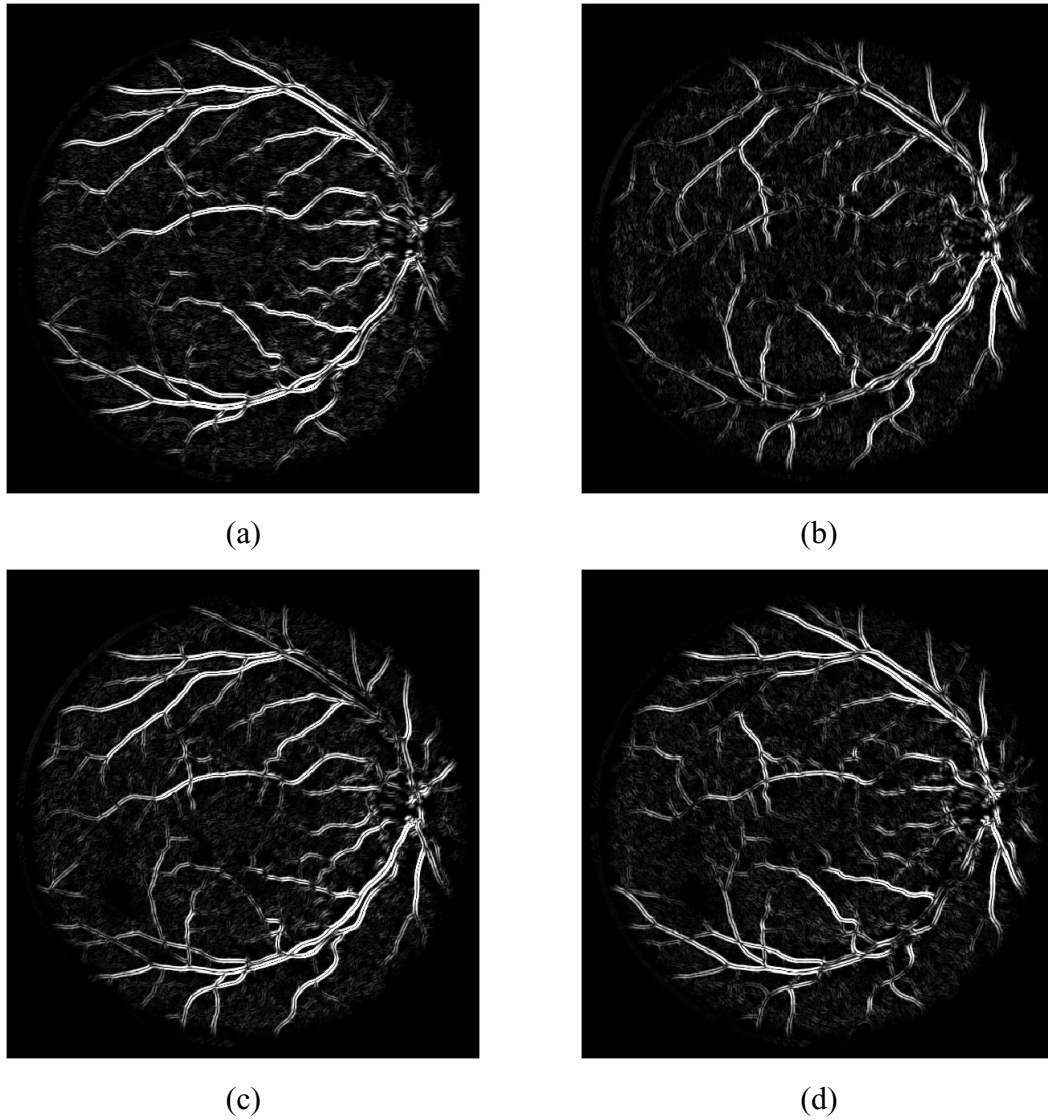


Figure 18: Potential vessel edges presented by the image gradients in (a) the horizontal: I_x , (b) vertical: I_y , (c) diagonal: I_z and (d) anti-diagonal: I_k orientations.

3.3. Introduction to Fuzzy Logic Systems

3.3.1. The Motivation for Proposing a Fuzzy Logic System

In every image segmentation technique, it is beneficial to define the background and the target according to the data. In this project, the retinal blood vessels are the targets whose region is a connected component, and the boundaries of the vessels are the set of pixels in the region with one or more neighbors out of the region.

Depending on the utilization of dominated features of the image, the segmentation methods can be divided into the region and edge-based methods [1]. Region-based methods search for similarities between adjacent pixels or voxels, and therefore, they represent homogeneous areas in an image. On the other hand, the edge-based methods employ several filters to cluster each pixel or voxel as edge or non-edge [2]. The procedure of extracting the features after applying the Robinson compass kernels in the previous section is an example of edge-based segmentation. Combining boundary-based and region-based methods can achieve an objective approach with better performance [3].

Medical image acquisition suffers from contamination of image with noise, leading to poor contrast between target, namely retinal blood vessels in this project and background. In many cases, the relationship between regions is defined to take uncertainties within the areas into account [2]. Fuzzy logic is a region-based method that

addresses the uncertainties using fuzzy rules. This processing technique combines information from the natural language of humans with measurements and mathematical formulation [14].

Most daily words and evaluations are not clearly defined mathematically. For more clarification, there are cases such as, "If it is sunny and warm today, I will swim." The terms 'sunny', 'warm' and 'swim' are called 'linguistic.' On the other hand, stochastic uncertainty states that there is a probability an event will occur or a statement is true, implying that there will be situations where uncertainty is present. Possibility theory is a mathematical expression that handles uncertainty and insufficient information. So, it can be argued that Stochastics and Fuzzy Logic complement each other.

It turns out that fuzzy logic is an excellent explanation for uncertainty scenarios. The fuzzy concept describes the system itself and calculates a safe margin of error to accept and still be accurate enough when producing results [73]. In the current research, this feature makes fuzzy logic an ideal solution in image segmentation applications, precisely, blood vessel detection. The fuzzy notions are required to characterize the image pixels because the vessels have indefinite and unclear boundaries.

While this project has been pursued by Interval Type-2 Fuzzy Logic (IT2 FL), it is worth providing a brief background of material about the type-1 fuzzy logic model and making the nature of the fuzzy expressions sensible.

3.3.2. Type-1 Fuzzy Inference System

A type-1 fuzzy set in the space of X is defined by a membership function $\mu(x)$, which takes values on the interval $[0,1]$ and can be represented by membership degrees of an element to the set [14]. Accordingly, zero is interpreted as a variable that does not belong to the set, while “one” refers to complete certainty that the variable is a set member given the corresponding membership function. The intermediate values may also show how to reach a degree that member belongs to the set [8].

3.3.3. Type-1 Fuzzy Membership Functions (MF)

Unlike classical sets, characteristic functions are used in fuzzy logic to show that the member belongs to the set. The point is that the classical groups are defined by distinctive functions and are followed by crisp variables which represent precise quantities such as “ $x = 3.14$ ” or “ $A \in \{0,1\}$ ”. Indeed, a proposition is either True or False, such as “ $A \times B \rightarrow C$ ”. Classical sets have two main requirements. One of the characteristics is that the members of each group are distinguishable from each other. Also, for any given object in the set, it can be specified whether the object is or is not a member of the group.

Fuzzy sets do not require sharp boundaries to separate the members from the other objects, and a membership function defines the relationships. It means they do not have

crisp definitive limits, and there will be some room for adjustment. By this definition, each member can belong to more than one set with a degree of membership [8].

A curve called a membership function can be obtained by plotting the members' degree of belonging, showing the elements' connection with each other. Because of its smooth transition, a fuzzy set better represents the model. The membership function can help identify the class of each member of the fuzzy set depending on its membership degree to each class.

A more convenient and concise way to define a membership function is to express it as a mathematical formula while the degree of membership of each element is between [0 1]. Subsequently, a fuzzy set of A has elements (y) on the universe of discourse U , that has a membership function of μ_A , which maps U to the membership space as:

$$A = \{(y, \mu_A(y)) \mid y \in U\} \quad (3.16)$$

Based on the problem, there are different shapes for the membership function. Figure 19 represents some of the commonly used functions.

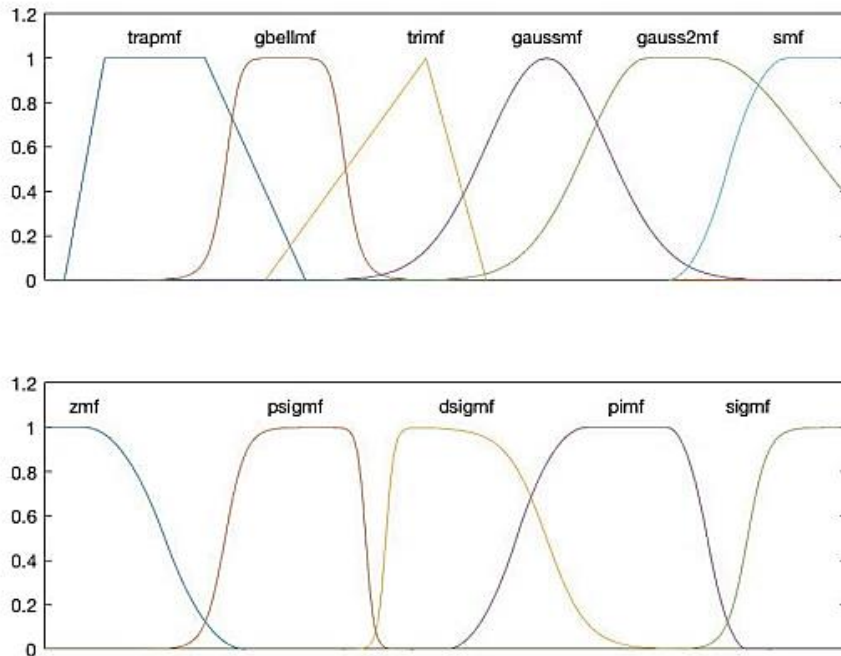


Figure 19: Fuzzy Membership Functions from MATLAB Fuzzy Logic Toolbox.

3.3.4. Linguistic Variables and Fuzzification

The process that maps each measured numerical input variable into a fuzzy set using the membership functions is called fuzzification. In fuzzy logic, linguistic variables transfer data, translate the physical environment, and make it meaningful for computers. Linguistic variables are essential to developing the fuzzy set theory. A linguistic variable is an operation whose values are words or sentences in a natural or artificial language [8,9]. Such a linguistic variable modifies fuzzy sets' shapes by adverbs such as very, high, and less.

3.3.5. Fuzzy Rules

Taking the linguistic variable of the fuzzy input and the corresponding linguistic variable of the fuzzy output, one can extract a fuzzy rule using “if...then” rules within which the physical world can be transferred into something that computers understand. The linguistic variables are connected using Boolean operators such as “OR” and “AND.” The first if-part is called premise or antecedent, and the second part, which is then-part, is called consequent [54]. Two types of Fuzzy Systems (FS) architecture differ in fuzzy rule consequents. In Mamdani systems, both antecedent and consequent are linguistic, while in the Takagi-Sugeno system, the consequent part is modelled by mathematical functions.

Under a sequence of conditions and arrangements, the system is called a rule-based system. Upon the observations and changes in variables, some characteristics are discerned, and then some system models are developed [8].

3.3.6. Inference Engine

This component decides which rule and to what degree to be fired at a time [54], and it is responsible for applying the fuzzy rules to the fuzzy input to generate the output. At this stage, the fuzzy “OR” operator is defined as the union of the fuzzy sets (X and Y) with respected fuzzy membership functions (μ_X and μ_Y), and it is given by the maximum of the membership functions [2]:

$$\mu_{X \cup Y} = \max(\mu_X, \mu_Y) \quad (3.17)$$

Moreover, the “AND” operator is calculated by the intersection of the fuzzy sets, which is the minimum of μ_X and μ_Y membership functions to compute a fuzzy output distribution [2].

$$\mu_{X \cap Y} = \min(\mu_X, \mu_Y) \quad (3.18)$$

Finally, the output distribution is computed by combining all the consequents based on the rule strength.

3.3.7. Defuzzifier

The aggregated fuzzy output sets from the inference engine are sent to the defuzzifier process to create a crisp output. The most common method of defuzzification is the centroid. The aggregation is performed by placing all membership functions on the same axis and combining them. The crisp value is found from the center of the area of the overlapped region [2]. Figure 20 represents a network of type-1 fuzzy inference systems.

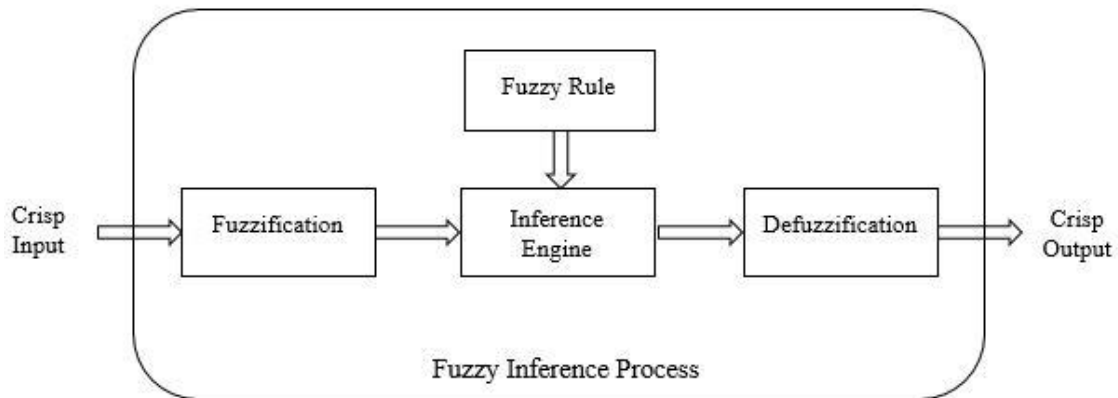


Figure 20: The components of a Type-1 Fuzzy Inference System [74]

3.3.8. Generalized Type-2 Fuzzy System (GT2 FS)

The shortcoming with the Type-1 fuzzy system is that the fuzzy inputs and outputs will become precise by which the system may not consider the uncertainties through membership values [54]. The type-2 fuzzy sets generalize type-1 models; however, the membership function values are the fuzzy sets in $[0, 1]$ for each pixel. Hence, the type-2 fuzzy sets are three-dimensional and characterized by a Footprint of Uncertainty (FOU) as the third dimension. Consequently, more freedom is provided to handle the membership function's uncertainties [54].

Assuming the values in the FOU as a new fuzzy set, we can associate them to a new membership function so that specific values can be weighted. Hence, the values are taken from the first membership function, called the primary membership function, and

then they are mapped to a new distribution by a secondary membership function. This secondary MF gives weights to the values from the primary MF. Lower and upper membership functions represent the primary MF, so they incorporate uncertainty about the membership function into fuzzy set theory [12,15,30, 54]. This notion is illustrated in Figure 21.

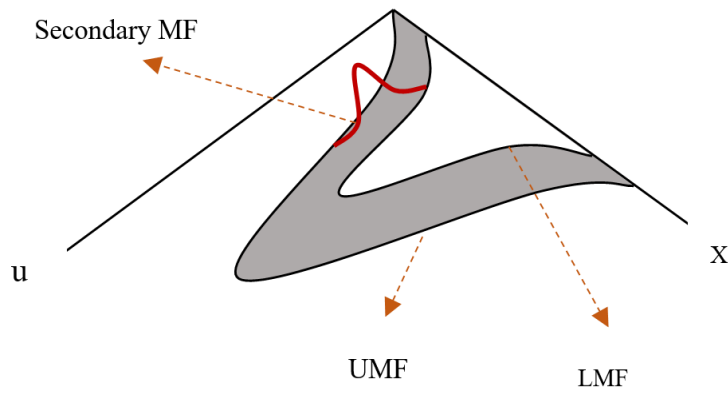


Figure 21. Generalized Type-2 Fuzzy Membership Function

Following this introduction to T2 FS, \hat{A} is denoted as a type-2 fuzzy set which is a bivariate function and is expressed by the mathematical notion below [69]:

$$\hat{A} = \{((x, u), \mu_{\hat{A}}(x, u)) \mid \forall x \in X, \forall u \in J_x \subseteq [0,1] \} \quad (3.19)$$

In a GT2 FS denoted by \hat{A} , the membership function $\mu_{\hat{A}}(x, u)$, takes the values in the range of [0 1] and $J_x \subseteq [0, 1]$ is called the primary membership function with the primary variable of x . The primary membership function consists of the lower and upper membership functions (LMF and UMF). As illustrated in Figure 21, the secondary

membership function is a vertical slice of $\mu_{\hat{A}}(x, u)$ with the same limited values between [0 1]. Besides, \hat{A} in continues space is expressed by [69]:

$$\hat{A} = \int_{x \in X} \int_{u \in J_x^u} \mu_{\hat{A}}(x, u) / (x, u) \quad (3.20)$$

As formerly stated, FOU is represented by a bounded region between the two primary MFs and is the 2-dimensional support of \hat{A} .

$$FOU(\hat{A}) = \{(x, u) \in X \times [0,1] \mid \mu_{\hat{A}}(x, u) > 0\} \quad (3.21)$$

In other words, the FOU is the sum of all primary membership functions of J , and it encloses unlimited numbers of fuzzy sets into its footprint of uncertainty [54,55].

$$FOU(\hat{A}) = \cup_{x \in X} J_x^u \quad (3.22)$$

The components in GT2 FS are identical to T1 FS except for the type reducer, which is essential for type-2 fuzzy systems to reduce the type. Then, the defuzzifier turns the fuzzy outputs into crisp values.

As discussed in the current section, it can be sensed that the three-dimensional generalized type-2 fuzzy system is more complicated than type-1 fuzzy systems and demands more mathematical computations. The type reducer step is the procedure with the most computational cost. According to Almaraashi, M *et al.* 2016 [69], this heavy computational complexity has limited this model's application in the real world. Several

methods are proposed to limit the complexity of these systems [54, 55, 69]. However, the system is still suffering from a considerable run time.

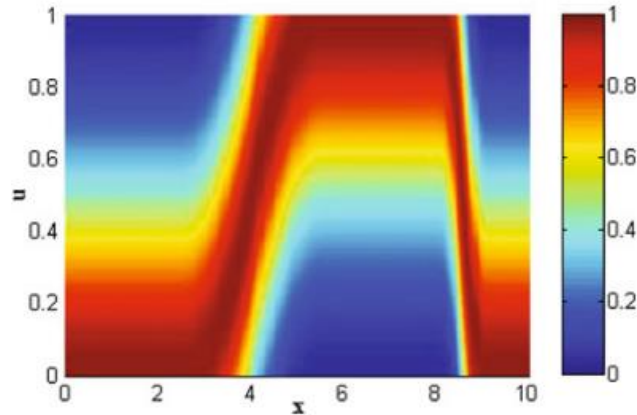


Figure 22. The footprint of Uncertainty in GT2 FS [54].

3.3.9. Interval Type-2 Fuzzy System (IT2 FS)

The notions described in the last section are dedicated to the Generalized Type-2 FS. When $\mu_{\hat{A}}(x, u) = 1$ for $\forall x \in X, \forall u \in J$, then \hat{A} is called an Interval Type-2 Fuzzy System (IT2 FS) [54]. So, the third dimension of GT2 FS is no longer needed, and the system is defined as equation (3.23).

$$\hat{A} = \int_{x \in X} \int_{u \in [0,1]} 1/(x, u) \quad (3.23)$$

The IT2 FS is the subset of GT2 FS with a more straightforward computation. In Figure 23, the FOU is represented in 2D and is described with upper and lower membership functions while the secondary grade or amplitude equals 1.

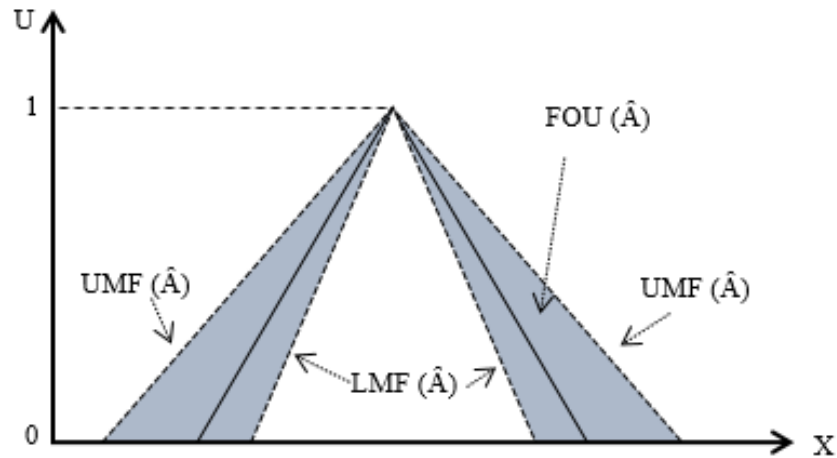


Figure 23: The footprint of Uncertainty (Shaded) for IT2FS

It has been proved that the IT2 FS outperforms the T1 FS due to the FOU that has tremendous potential to model and handle the uncertainties and finally make better performance [54, 55]. In the meantime, the GT2 FS is no less accurate than IT2 FS [54, 55, 69]. However, despite all the efforts to restrict the computations in generalized type-2 fuzzy systems, they are still tedious due to their complexity of being applied in real life.

In [69], the authors made attempts to answer whether the GT2 FS has better performance than IT2 FS in tackling the uncertainties in four different problems. Two type reduction techniques have been evaluated: the sampling method and vertical-slices centroids type-reduction. In addition, the IT2 FS has been tried for the same problems, and the results have been reported. The GT2 FS with sampling type reducer has the same performance as IT2 FS, while the running time was about 21 times more. Meanwhile, although the other deterministic type-reduction method obtained better results for all

problems, the execution time remained challenging. Numerous control problems have been undertaken using Mamdani IT2 FS [54]. Moreover, several pieces of research are being conducted to investigate the application of IT2 FS in diverse aspects of image processing [70]. As a result, this method has been developed to form a new system for detecting the blood vessels in fundus images.

The steps to reach from input to output in IT2 FS are similar to the T1 FS. Firstly, the crisp inputs are fuzzified to the IT2 inputs. Then, using the same rules as T1 FS, the inference engine activates to produce IT2 FS output. A type reducer is required to project the T2 model to T1 FS. A type reducer is an interval type-1 fuzzy set, made by the centroid of the type-2 fuzzy set, estimated from the upper and lower membership functions. This method is called the Enhanced Karnik–Mendel Algorithm (EKM), an iterative type-reduction procedure widely used in fuzzy logic theory, especially in IT2 FS [58]. Finally, the T1 FS output is defuzzified to make the crisp output [54]. The mentioned steps are briefly described in Figure 24.

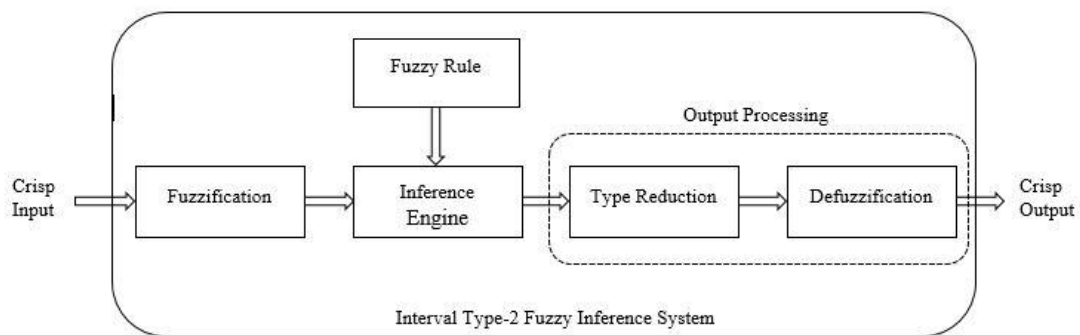


Figure 24: Architecture of IT2 FIS [75]

3.4. Proposed Fuzzy Logic Algorithm

Following the provided introduction to different Fuzzy Inference Systems (FIS) types, the proposed methodology is designed as a Mamdani IT2 FS with four crisp I_x , I_y , I_z and I_k inputs, and one crisp output detects the edges. Each input has three type-2 Gaussian membership functions with ‘Low,’ ‘Medium,’ and ‘High’ linguistic variables. Equation (3.24) describes the IT2 Gaussian membership function where i refers to either x , y , z or k directions and j takes either *Low*, *Medium* or *High* variables.

$$\mu(x, [\sigma_i, m_{ij}]) = \exp \left[-\frac{1}{2} \left(\frac{x - m_{ij}}{\sigma_i} \right)^2 \right] \quad (3.24)$$

The upper membership function is characterized by two parameters which are sigma and mean (σ_i, m_{ij}). In this step, it was realized that to optimize the membership functions; they should be adapted to the range of gray tones of the corresponding image. For this purpose, the mean and sigma values are formulized concerning the input image. As a result, the sigma and the mean parameters of the Gaussian membership functions are calculated using the following equations.

$$m_i^{Low} = \min(I_i) \quad (3.25)$$

$$m_i^{High} = \max(I_i) \quad (3.26)$$

$$m_i^{Medium} = \frac{m_i^{High} - m_i^{Low}}{2} \quad (3.27)$$

$$\sigma_i = m_i^{High} / 5 \quad (3.28)$$

As mentioned earlier, I_i takes input features in that I_x , I_y , I_z , or I_k . According to the corresponding component, m_i^{Low} is the mean value of Gaussian MF of the ‘Low’ linguistic variable, m_i^{High} is the mean value of Gaussian MF of the ‘High’ linguistic variable and m_i^{Medium} is the mean value of Gaussian MF of the ‘Medium’ linguistic variable. Moreover, the value of σ_i is a shared constant for all linguistic variables of each fuzzy input and is calculated by (3.28).

To create the footprint of uncertainty in MATLAB, the lower membership function is set by a scaling factor that is a scalar between 0 and 1. This factor specifies the peak of LMF. Indeed, a delay factor indicates that the LMF value increases from zero. The scaling and delay factor values have been set to 0.9 and 0.09, respectively. After evaluating the intensities of fuzzy inputs, it has been determined that the range of [0 6] covers the input pixel values. Figure 25 shows the originality of the shapes of MFs for an image from DRIVE test data.

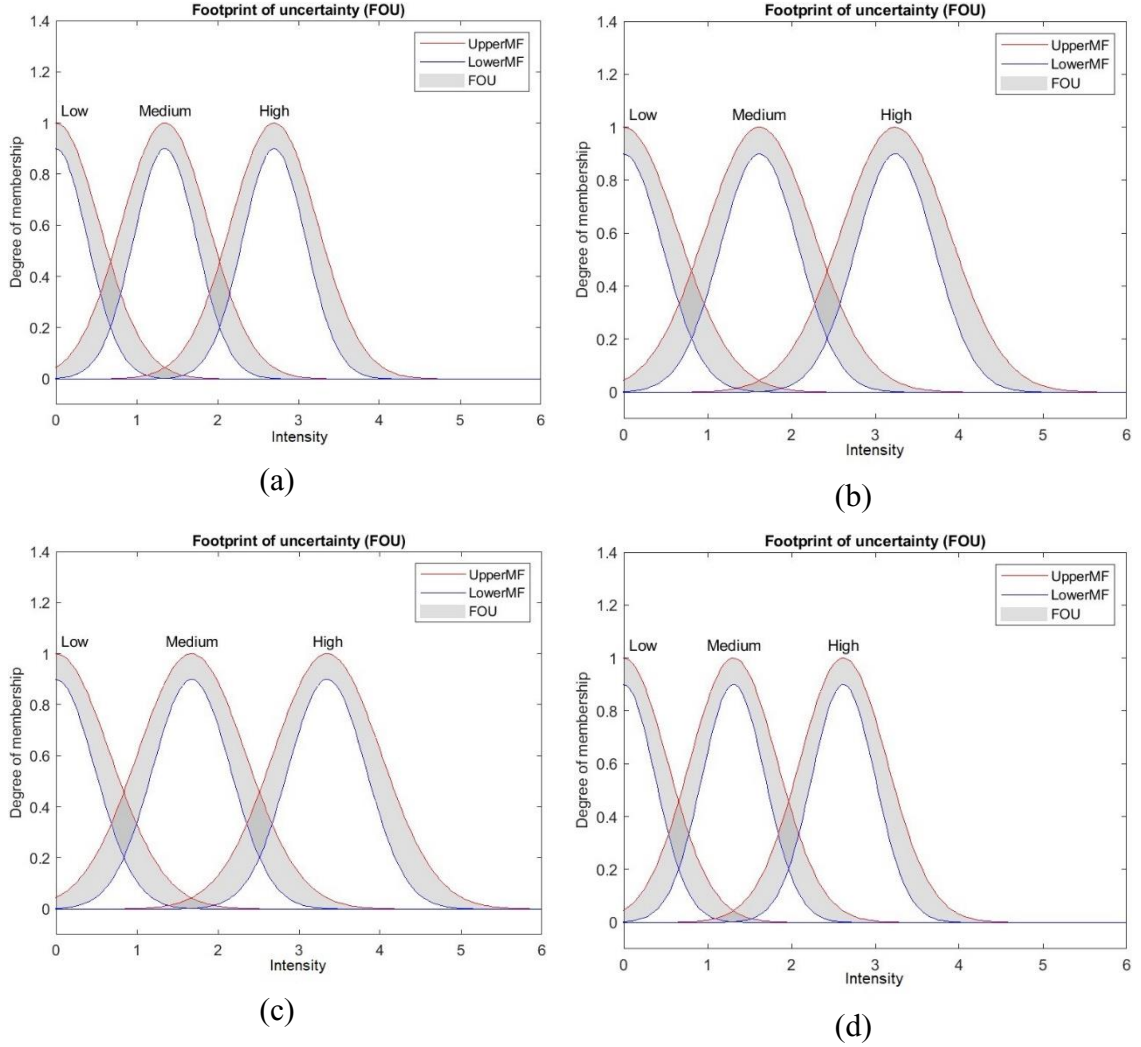


Figure 25: The membership functions of pixel intensities of four crisp inputs of the proposed IT2 FS, implemented in MATLAB for an image from DRIVE test data. (a) I_x , (b) I_y , (c) I_z , (d) I_k .

In the next task, the output of the FIS must be defined. Two linguistic values of ‘Edge’ and ‘No-Edge’ have been described. The result was normalized to the range of [0 1]. The mean values of the Gaussian membership functions are set to one and zero to address the ‘Edge’ and ‘No-Edge’ variables. The sigma value for both membership

functions is the constant of $1/4$. The scaling and delay factors were set to 0.9 and 0.09 to create the FOU and model uncertainty in the degree of membership.

The choices for the constant values concerning the scaling and delay factors and sigma have been adjusted based on the best accuracy performance on the DRIVE dataset.

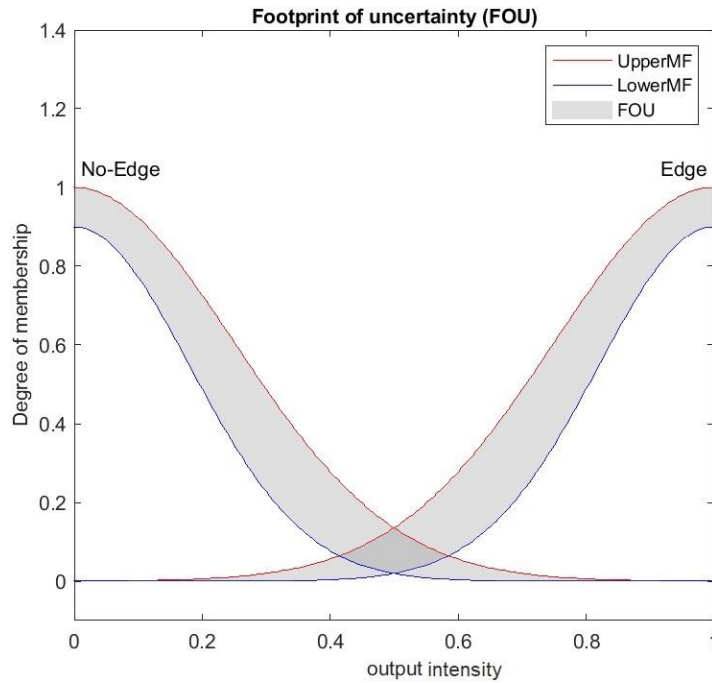


Figure 26: Proposed IT2 output membership function

The next step is to model the fuzzy inference rules. In this part, three rules have been defined to extract the edges from the existing relationship between the image gradient features by the antecedents and consequents expressed in Table 1.

TABLE 1: Designed Fuzzy Rules for the IT2 fuzzy system

Rule	Input				Operator	Output
	I_x	I_y	I_z	I_k		
1	<i>High</i>	<i>High</i>	<i>High</i>	<i>High</i>	<i>OR</i>	<i>Edge</i>
2	<i>Medium</i>	<i>Medium</i>	<i>Medium</i>	<i>Medium</i>	<i>OR</i>	<i>Edge</i>
3	<i>Low</i>	<i>Low</i>	<i>Low</i>	<i>Low</i>	<i>AND</i>	<i>No-Edge</i>

In the evaluation stage, the algorithm examines the rules to classify every pixel in the field of view. Therefore, the union of the results from the three mentioned rules makes the output membership function of the corresponding pixel. The fuzzy output needs to turn into the crisp output in the defuzzification step. Beforehand, the type reduction method of the Enhanced Karnik–Mendel Algorithm (EKM) is applied to the outcome of the fuzzy inference engine to turn the type-2 fuzzy outputs to type-1 by calculating the centroid of the type-2 fuzzy set from the upper and lower membership functions. After type reduction, the centroid method is applied as the most common defuzzification technique that returns the center of the area under the combined output membership function [31] and provides us with the crisp output.

The output of the fuzzy logic algorithm is indicated in Figure 27(c). As it can be seen, the proposed type-2 FIS was able to extract most edges of the blood vessels.

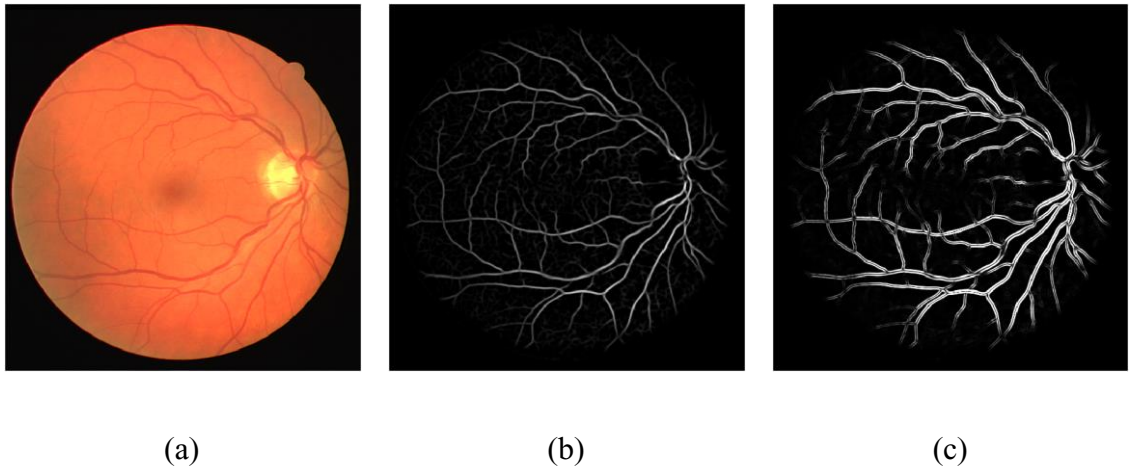


Figure 27: (a) The original fundus image from the DRIVE dataset, (b) Result of pre-processing, (c) Output of IT2 FS

3.5. Post-processing

The output of the fuzzy logic model is a grayscale image with values in the range of $[0,1]$ which mainly contains the edges of the blood vessels. Finalizing the segmentation methodology and evaluating the method's performance demand the binary image. Besides, morphological refinements combine the blood vessels in the binary image and remove the noise.

3.5.1. Image Binarization

Binarizing the medical image can be defined as taking a grayscale image and converting it to a black-and-white one. This process is being done to limit the image

information to the region of interest only. In this case, the binary image must contain the retinal vessels as one, while the rest of the data is considered background and is set to zero.

Over the years, there have been countless methods for image binary segmentation which can be categorized into global and local thresholding [28]. Global strategies, such as Otsu, apply only one threshold to the image, resulting in a binarized picture with some loss of essential information. However, single thresholding may not be perfect for keeping the details of the vessels' boundaries. For this reason, hysteresis thresholding can be applied to the image as the binarization step. This approach applies two thresholds to the image: high and low. In the first step, the method selects the regions above the high threshold. Then, the surround pixels with eight connectivity are searched, and areas above the low threshold are kept, given that they are connected to those above the high threshold [32].

The low and high thresholds are selected experimentally and according to the histogram of fuzzy output distribution. The distribution of the intensities is firstly rescaled to the intervals of $[0, 1]$. This rescaling ensures that any image's histograms that are not starting from zero are pushed back to the origin. Later, the image's histogram is examined to develop the threshold limits. Different factors have been considered in selecting the threshold values, including accuracy, sensitivity, and the density of falsely detected pixels. Finally, the low and high thresholds of the hysteresis were set as 0.045 and 0.05, respectively. Empirically, it has been noticed that changing the hysteresis limits results in

slightly higher accuracy at the cost of losing sensitivity. Since sensitivity is the measure of correctly detected blood vessels, it is more favorable to consider this metric as the primary measure of the algorithm performance. The higher number of true positively classified pixels is informative in detecting the early stages of DR. An example of the gray tone distribution, and binarization result is indicated in Figure 28.

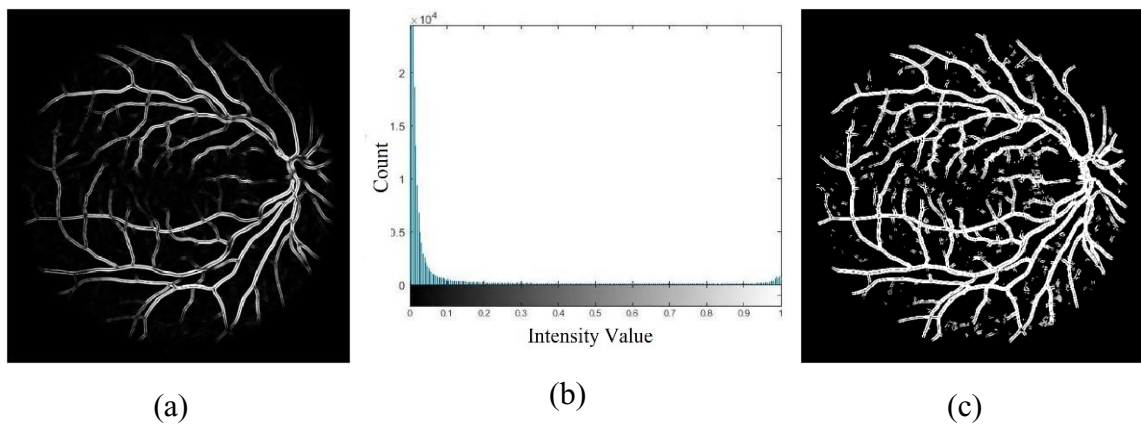


Figure 28: (a) IT2 FS output image, (b) Histogram plot of fuzzy output, (c) Binarized image

3.5.2. Morphological Discovery

Binary images may carry various imperfections that impose noise or unwanted textures on the image. For this reason, morphological operations are applied to remove these noises to a great extent. The function uses a structuring element that defines the region of interest or neighborhood. There are two fundamental morphological operators, namely called, erosion and dilation.

3.5.2.1. Erosion

As described in (3.29), the erosion (denoted by \ominus) of a binary image A in set Z by a structuring element B can be defined as B 's translations that entirely fit the input image A [2]. According to this definition, erosion is helpful to remove small noises from a binary image while simultaneously reducing the size of regions of interest.

$$A \ominus B = \{Z \mid (B)_Z \subseteq A\} \quad (3.29)$$

3.5.2.2. Dilation

The dilation (denoted by \oplus) of a binary image A in set Z by a structuring element B is the translation of B that intersects with at least one pixel of A [2]. Dilation has the opposite effect of erosion, and it expands both the inner and outer boundaries of regions.

$$A \oplus B = \{Z \mid (\hat{B})_Z \cap A \neq \phi\} \quad (3.30)$$

3.5.2.3. Closing

The process of a dilation followed by erosion is called the closing (denoted by \bullet). Following the expansion and shrinkage by the operators, the closing can keep the initial region sizes

[2]. Furthermore, the closing operator can remove pepper noise and fill the gaps in bright areas.

$$A \bullet B = (A \oplus B) \ominus B \quad (3.31)$$

3.5.2.4. Morphological Processing on Binary Image

Following the above descriptions, the closing operation fills the holes and detects more potential vessel pixels. Because the observed black pixels within the vessels tend to be small discrete regions, the disk structuring element with a one-pixel diameter was sufficient for the closing procedure. The effect of the closing operation on vessel gaps has been illustrated in Figure 29. After using the closing operator, morphological erosion with a square-shaped structuring element of three is used to remove the noise and shrink the vessels to force the vessel diameter to follow the ground truth.

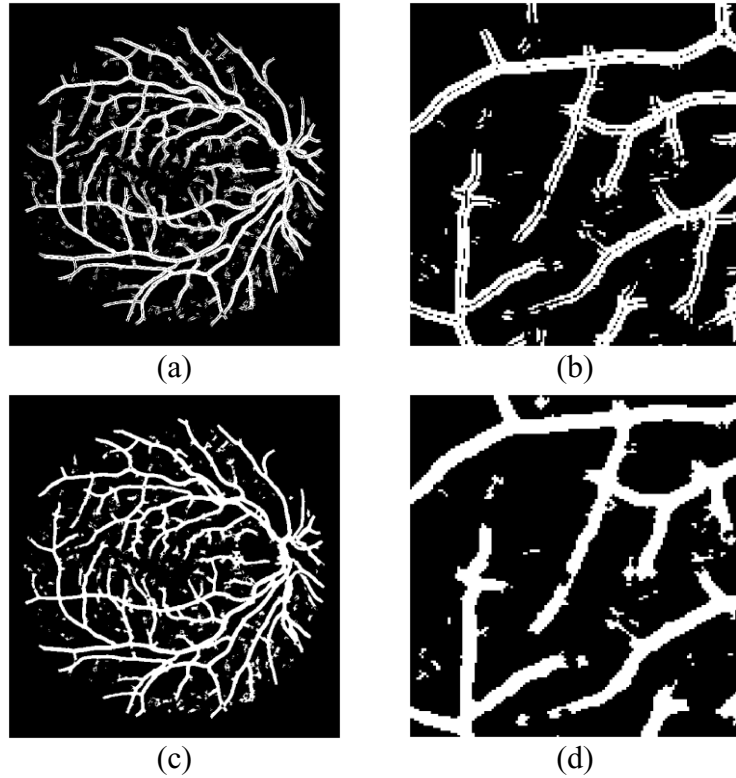


Figure 29: Comparison of blood vessels images before (a and b) and after (c and d) applying closing operation. (b) and (d) are the magnified copies of (a) and (c), respectively.

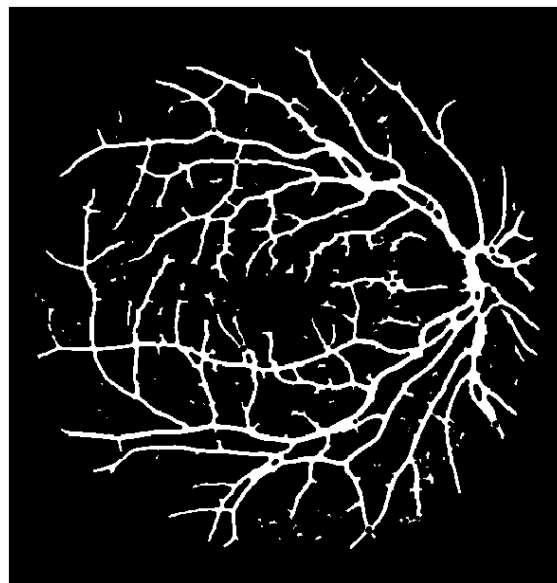


Figure 30: The result of erosion applied to the binarized image from Figure 29(c)

3.5.3. Connected Component Analysis

The last part of the methodology tried to remove unwanted noise that remained in the binary image. For this goal, according to the connectivity in 8 connected objects, pixels of the image are grouped in different labels. The number of pixels in each element is counted. Following this method, the components with very few pixels can be ignored as they are more likely to be unwanted noise. By analyzing the distribution of Connected Components (CC) in images, the pieces smaller than 10 pixels have been ignored.

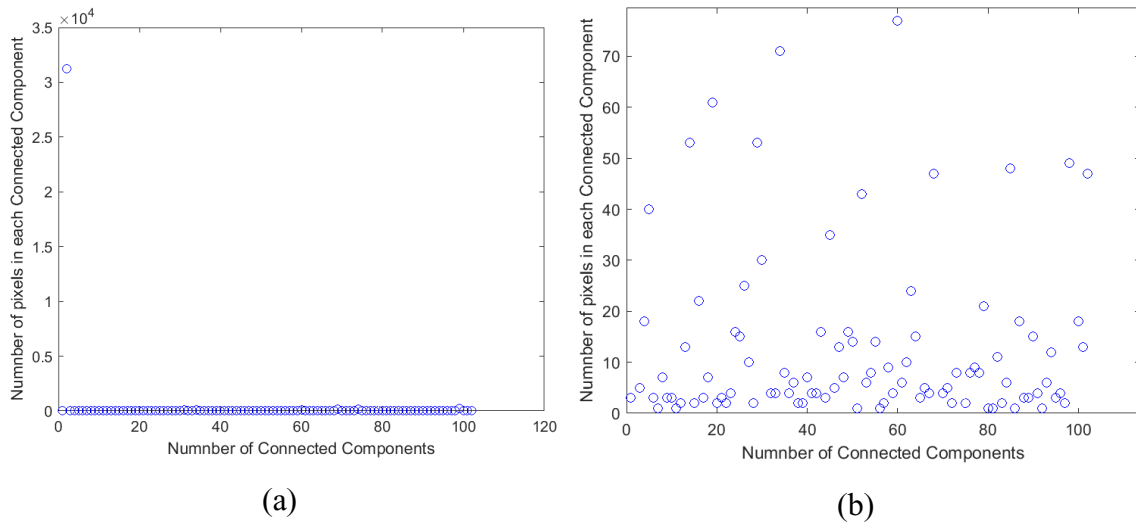
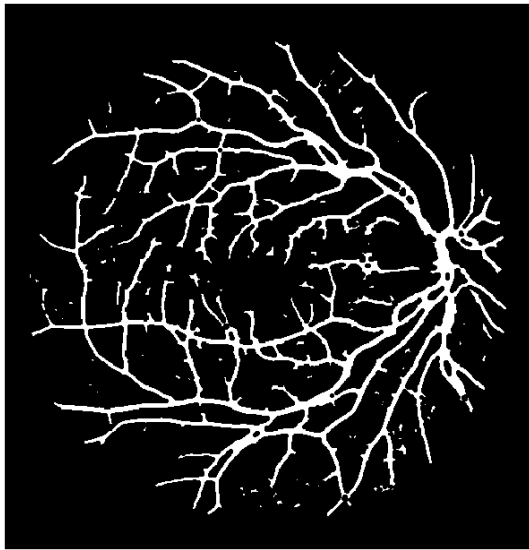


Figure 31: (a) Distribution of connected components, and (b) its magnified plot

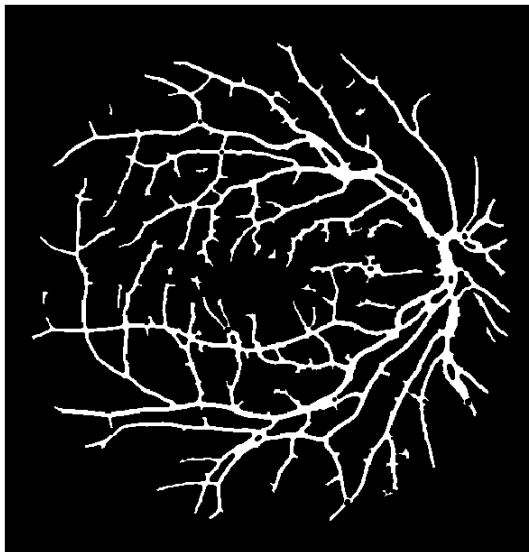
After being analyzed from the view of connected components, the eroded image is demonstrated in Figure 32.



(a)



(b)



(c)



(d)

Figure 32: Visual comparison of the eroded image before (a, b) and after (c, d) CC analysis

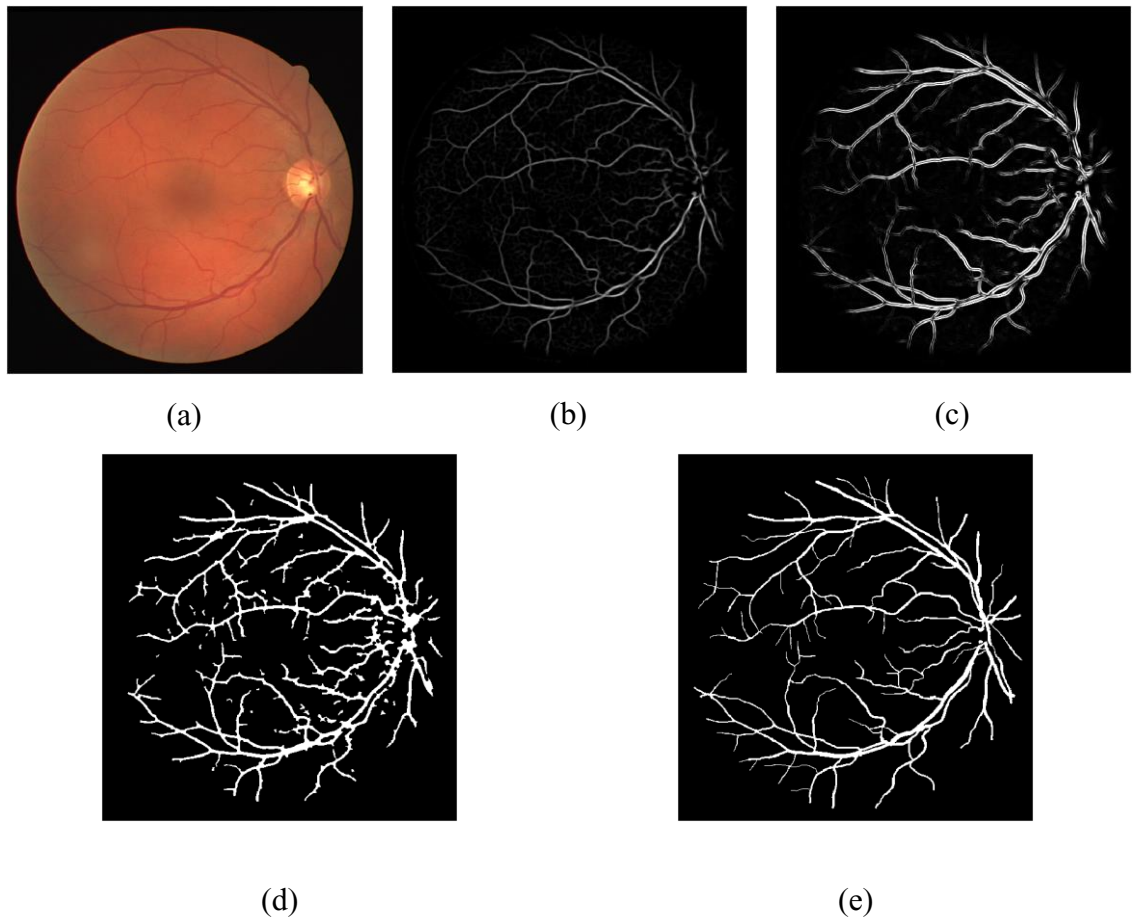


Figure 33: (a) Original fundus image, (b) Pre-processed image, (c) Output of IT2 FS, (d) Final Segmented Image, (e) Ground truth image

Chapter 4: Simulation Results

4.1. Database

The proposed retinal vessel extraction algorithm is evaluated using a publicly available retinal image DRIVE (Digital Retinal Images for Vessel Extraction) database [44]. This database consists of a total of 40 color fundus photographs. The photographs were obtained from a diabetic retinopathy screening program in the Netherlands comprised of 453 subjects between 31 and 86 years of age. All images have been taken with a Canon CR5 nonmydriatic 3CCD camera with a 45-degree field-of-view (FOV) and saved in JPEG format. Each image was captured at the image size of 565 by 584 pixels using 8 bits per color plane. This standard database enables comparison with the pieces of literature.

This database includes two sets of training and test, each containing 20 images. The training set involves the corresponding FOV masks and a human expert's single manual

vessel segmentation for each image that is accounted for as the ground truth results. The respective ground truth images are finally used to evaluate the algorithm performance. Also, the measures compare the results with other existing retinal blood vessel segmentation algorithms (using the same DRIVE database).

The test set includes 20 images for which two manual segmentations were available. The first observer result set is the gold-standard segmentation upon which the performance of the articles is revealed. The second observer's results are compared with the segmentation of the first one. Furthermore, a mask image is available for every retinal image, indicating the region of interest.

4.2. Performance Measures

4.2.1. Confusion Matrix

The outcomes of the algorithm are compared with the ground truth images of the DRIVE database. This section presents some metrics to measure the quality of the vessel detection method.

The confusion table is first made to represent the misclassified and correctly classified instances, namely the pixels in the binary output of the algorithm. According to the confusion matrix and to evaluate a standard machine learning model, the pixels in the

predicted segmented image are categorized into four groups by considering the blood vessel's pixels as the positive instances. The mentioned categories are True Positive (TP), True Negative (TN), False Positive (FP) and False Negative (FN), where TP is the number of blood vessels correctly detected, TN is the number of non-blood vessels correctly identified, FP is the number of non-blood vessels wrongly seen as vessels, and FN is the number of blood vessel pixels incorrectly detected as non-vessel.

		Actual Class	
		Positive	Negative
Predicted Class	Positive	TP	FP
	Negative	FN	TN

Figure 34: Confusion matrix for multi-class machine learning models. The parameters indicate True Positive (TP), False Positive (FP), False Negative (FN) and True Negative (TN)

Subsequently, for the dense prediction task of image segmentation, the following metrics are defined:

$$Acc = \frac{TP+TN}{TP+TN+FP+FN} \quad (4.1)$$

$$Se = \frac{TP}{TP+FN} \quad (4.2)$$

$$Sp = \frac{TN}{TN+FP} \quad (4.3)$$

$$Jaccard = \frac{TP}{TP+FP+FN} \quad (4.4)$$

$$Dice = \frac{2TP}{2TP+FP+FN} \quad (4.5)$$

In the presented measurements, accuracy (*Acc*) reports the percentage of pixels in the image which are correctly classified. Sensitivity (*Se*) represents the number of blood vessel predictions of all vessels in the ground truth, and specificity (*Sp*) measures how well the model can identify non-blood vessel pixels. The *Jaccard* index quantifies the percentage overlap between the ground truth mask and the predicted vessels in the binary image. Furthermore, the *Dice* coefficient is a statistic metric that measures the similarity of two samples by calculating the area of overlap divided by the total number of pixels in predicted and ground truth images.

Since each metric has shortcomings and each measure captures a different similarity between the result and the gold-standard image, it is usual to combine them in the report to infer conclusions. While sensitivity and specificity ignore FP and FN errors, respectively, accuracy shows the ability of the method to differentiate the blood vessels and the non-vessels. However, dice and Jaccard indices are also favorable when the ground truth image is available. Due to the size of the blood vessels' pixels compared with the

extensive background region, a class imbalance has been observed where the Jaccard index or so-called the Intersection over Union (IoU) would be more robust to this issue and gives an insight regarding overall performance.

4.2.2. Quality Measurement Using MSE and PSNR Indices

To compare the cumulative squared error between the proposed method and the ideal edges, the Mean Square Error (MSE) can be the error metric. Assuming the images have $m \times n$ pixels and the original image and the processed image are denoted by J and K ; respectively, MSE can be calculated from the equation below [71]:

$$MSE = \frac{1}{mn} \sum_{i=1}^m \sum_{j=1}^n [J(i, j) - K(i, j)]^2 \quad (4.6)$$

The PSNR metric represents the Peak of the Signal-to-Noise Ratio between the detected image and the ground truth, expressed as a decibel. So, the higher the value of PSNR, the better the quality of the algorithm [15].

$$PSNR = 10 \log_{10} \left(\frac{(MAX_J)^2}{MSE} \right) \quad (4.7)$$

The measures mentioned above consider the pixels in the FOV only. Generally, reviewing other related works based on each of the above metrics provides one with a view of the method's behavior.

4.3. Simulation Results

Simulation has been performed in MATLAB R2019b using the image processing toolbox. The system was an Intel ® Core™ i72670QM CPU @ 2.2 GHz with 12 GB of RAM running Windows 10. In Table 2, the proposed model is evaluated using the DRIVE test data, and the performance metrics and execution time per sample are reported.

TABLE 2: Performance results on DRIVE test data

Image #	<i>Acc</i>	<i>Se</i>	<i>Sp</i>	<i>Dice</i>	<i>Jaccard</i>	<i>MSE</i>	<i>PSNR</i>	Execution time (Sec)
1	0.9515	0.8143	0.9649	0.7496	0.5995	0.0485	13.1388	5.248
2	0.9523	0.7549	0.9748	0.7641	0.6183	0.0477	13.2126	5.869
3	0.9384	0.7264	0.9618	0.7015	0.5402	0.0616	12.1011	5.277
4	0.9541	0.6707	0.9828	0.7290	0.5735	0.0459	13.3839	5.327
5	0.9561	0.6464	0.9882	0.7342	0.5800	0.0439	13.5796	5.248
6	0.9508	0.6510	0.9832	0.7205	0.5631	0.0492	13.0833	5.144
7	0.9468	0.6658	0.9751	0.6959	0.5337	0.0532	12.7436	5.137
8	0.9497	0.7107	0.9721	0.7084	0.5485	0.0503	12.9807	5.485
9	0.9567	0.7030	0.9791	0.7245	0.5680	0.0433	13.6328	5.175
10	0.9535	0.7323	0.9733	0.7214	0.5643	0.0465	13.3218	5.243
11	0.9443	0.7118	0.9672	0.6960	0.5337	0.0557	12.5435	5.163
12	0.9383	0.7723	0.9540	0.6838	0.5196	0.0617	12.0996	5.235
13	0.9435	0.7303	0.9666	0.7167	0.5585	0.0565	12.4830	5.607
14	0.9401	0.7937	0.9529	0.6817	0.5171	0.0599	12.2230	5.633
15	0.9479	0.7815	0.9607	0.6821	0.5176	0.0521	12.8296	5.160
16	0.9512	0.8031	0.9659	0.7482	0.5977	0.0488	13.1150	5.150
17	0.9421	0.7880	0.9563	0.6968	0.5346	0.0579	12.3734	5.154
18	0.9474	0.8395	0.9567	0.7168	0.5586	0.0526	12.7936	5.605
19	0.9592	0.8361	0.9704	0.7728	0.6298	0.0408	13.8961	5.031
20	0.9540	0.8250	0.9642	0.7251	0.5687	0.0460	13.3716	5.170

Table 3 represents the reported measures' average, maximum, and minimum values.

TABLE 3: Descriptive statistics on the performance measures reported in Table 2

Value	<i>Acc</i>	<i>Se</i>	<i>Sp</i>	<i>Dice</i>	<i>Jaccard</i>	<i>MSE</i>	<i>PSNR</i>	Execution time (Sec)
Max	0.9592	0.8395	0.9882	0.7728	0.6298	0.0617	13.8961	5.8694
Min	0.9383	0.6464	0.9529	0.6817	0.5171	0.4080	12.0996	5.0318
Mean (Std)	0.9489 (0.0062)	0.7478 (0.0621)	0.9685 (0.0101)	0.7185 (0.0263)	0.5612 (0.0323)	0.0511 (0.006)	12.9453 (0.5222)	5.3035 (0.2187)

4.4. Model Evaluation

It is challenging to determine the best methodology and compare the algorithms for the best segmentation approach [26]. However, this study relies on the mutual published measures on the same samples compared with ground truth images.

Table 4 represents the performance result of the proposed method and related recent works on the standard benchmarks of fundus images from the DRIVE database. As previously discussed in chapter 2, the vessel segmentation methods divide into supervised and unsupervised methods. So, to validate the proposal, the outcomes of the approach were compared with available works on the same database, separated into noted classes. Since most of the previous results were reported based on average accuracy, sensitivity and specificity, the same measures were considered in the following table.

TABLE 4: Comparison between the proposed method and related works in terms of average values of accuracy, sensitivity and specificity

<i>Category</i>	<i>Method</i>	<i>Se (%)</i>	<i>Sp (%)</i>	<i>Acc (%)</i>
	2nd. observer	77.57	98.19	94.73
<i>Supervised</i>	Liskowski <i>et al.</i> 2016 [50]	71.58	98.10	96.46
	Staal, J., <i>et al.</i> 2004 [41]	71.94	97.73	94.41
	Marín <i>et al.</i> 2011 [66]	70.67	98.01	94.52
	Fraz <i>et al.</i> 2012 [49]	74.06	98.07	94.80
	Ricci <i>et al.</i> 2007 [43]	-	-	95.95
	Soares <i>et al.</i> 2006 [52]	72.8	97.2	94.0~
<i>Unsupervised</i>	Bibiloni <i>et al.</i> 2019 [26]	72.10	97.00	93.80
	Kumar <i>et al.</i> 2020 [47]	75.03	97.17	94.32
	Kromer <i>et al.</i> 2016 [38]	67.45	97.14	93.34
	da Rocha <i>et al.</i> 2020 [48]	81.06	95.93	94.62
	Orujov <i>et al.</i> 2020 [20]	83.8	95.7	93.90
	B. Yildirim. 2015 [31]	72.28	97.04	93.82
	Zana <i>et al.</i> 2001 [53] *	66.9	98.3~	94.3~
	Bankhead <i>et al.</i> 2012 [68]	74.5	95.8	93.71
	K. Khatter <i>et al.</i> 2020 (Method I) [57]	-	-	92.62
	K. Khatter <i>et al.</i> 2020 (Method II) [57]	-	-	93.71
	Al Shehhi <i>et al.</i> 2016 [65]	85	94.4	93.4
	Chaudhuri <i>et al.</i> 1989 [46] *	-	-	87.73
		Proposed Method	74.78	96.85
* The result is taken from [47]				
* The result is taken from [76]				

Chapter 5: Discussion

5.1. Evaluating the results

According to Table 3, the proposed method has an accuracy of 94.89%, with a slight standard deviation of 0.006. Based on the recorded measures by the recent articles in Table 4, the obtained result achieved the highest accuracy through the current important supervised and rule-based methods. Besides, the accuracy is comparable with many of the supervised practices. As formerly mentioned in chapter 2, the supervised techniques are expected to achieve higher performance due to being trained by the model. At the same time, it must be considered that their performance on a new database is debatable.

From the supervised methods, Liskowski, Pawel *et al.* (2016) [50] gained the best accuracy on the DRIVE test set while the sensitivity of the suggested method outperforms

their model. It turns out that the proposed model is more capable of detecting the pixels relating to the blood vessels as the true positive instances.

The result of the current method stands on top of the ridge-based method proposed by Staal J. *et al.* (2004) [41], in both sensitivity and accuracy as two crucial measures to illustrate the correct classification of blood vessels pixels. Besides, the suggested model could tackle the problems of coarse region segmentation and false detection in FOV boundaries. Such proficiencies can be investigated in Figures 36 and 37. Furthermore, the authors stated that their primitive-based method has a running time of 15 minutes that is mainly spent in the classification stage. In contrast, the suggested model segments the image in about 5 seconds.

The survey of Marín, D. *et al.* (2011) [66] had lower performance on both sensitivity and accuracy, as well. According to their report, the worst result with the least accuracy was recorded on the 8-th image with a sensitivity of 0.5704 and accuracy of 0.9388. The proposed algorithm has sensitivity and accuracy values of 0.7107 and 0.9497, respectively, on the same image. Also, the maximum sensitivity of the method is 0.8139, whereas the current study has the highest record of 0.8395. In the meantime, the maximum accuracy of their model is 0.9602 with a sensitivity of 0.8058 on the 19-th image. The proposed study reached a higher sensitivity of 0.8361, with only 0.001 loss of accuracy, on the same image. As mentioned in [49], the model's accuracy on DRIVE test data with cross-training was 94.48%.

According to Soares *et al.* 2006 [52], it is observable that the proposed model has better performance in terms of both sensitivity and accuracy. According to [49], the average accuracy of the work by Soares with cross-training is 93.97%. The main drawback of the system was the long runtime of 9 hours to estimate the model's parameters while the model had difficulty segmenting the blood vessels in the area of the optic disk.

Comparing the current method with Fraz *et al.* 2012 [49], it can be argued that the methodology overtakes the results of the mentioned authors in both accuracy and sensitivity while they ended up with lower average accuracy of 94.56% with cross-training.

In Ricci *et al.* [43], the sensitivity and specificity were not measured, which is the limitation of the work as it disregards other criteria. However, despite the mentioned accuracy, the reported cross-training average accuracy is 92.66%, just below the obtained value in the proposed model [49].

In general, it can be discussed that the proposed algorithm had lower accuracy on only two of the presented supervised models before cross-training (that usually lowers the performance of the supervised algorithms). Nevertheless, the obtained accuracy is comparable with the state-of-the-art supervised models. Based on the acquired sensitivity, it can be stated that our introduced methodology had a better vessels' pixel prediction than the reviewed supervised method. This proficiency makes the proposed approach efficient in applications such as DR diagnosis, in which the region of blood vessels becomes essential.

By comparing the results of the method with the unsupervised models, it can be stated that the algorithm was more promising in extracting the blood vessels than the morphological processing proposed by Bibiloni, Pedro, *et al.* 2019 [26] in terms of both sensitivity and accuracy. While the specificity is only 0.15% lower, the accuracy and sensitivity are considerably greater than their method.

Kumar *et al.* (2020) [47] reported the lowest accuracy on image 3 with a value of 0.9339, while the proposed algorithm obtained an accuracy of 0.9384 on the same image. Furthermore, in the DRIVE test data set, image 8 is a pathological image caused by the breakdown of the blood vessel barrier leading to hard exudate. The authors reported an accuracy of 93.93%, while the current method achieved an accuracy of 94.97% on this same image. This result proves that the proposed method works better than this algorithm for detecting blood vessels in pathological images. A visual comparison between the segmented outcome from the authors' approach and the proposed methodology confirms that the suggested method was more successful in exposing fine vessels with low contrast.

The unsupervised method was proposed by Kromer, Robert, *et al.* (2016) [38] based on morphological processing and binarizing the image using the thresholding technique. This method gained lower sensitivity and accuracy.

According to da Rocha *et al.* (2020) [48], the sensitivity of their model based on the 2D Gabor wavelet transform has been higher than the suggested method in the cost of

lower accuracy and specificity. However, the reported values are on all test and training samples, making the initial data different from the current survey.

The article of Orujov F. *et al.* (2020) [20] is the only work on the higher order of fuzzy logic for segmentation of retinal blood vessels. The reported measures are based on 40 instances from training and test DRIVE data, making the comparison biased. According to the presented outcomes by the authors, the resulted images consist of a large diameter mask of the blood vessels while many of the details corresponding to the fine branches were lost. Figure 35 compares the segmented images resulting from [20] with the suggested method. From this figure, it is noticeable that the outcome of [20] is less accurate in the optic disk area and predicting the thinner vessels. Another drawback of [20] was the inability of their method to distinguish the adjacent vessels. This issue is illustrated in the bottom row of Figure 35.

The proposed IT2 FS has made several adjustments on different levels of the fuzzy algorithm, including adapting the membership functions' parameters to the corresponding image intensities and the new fuzzy rules. Besides, defining the Gaussian shape for the fuzzy outputs provides more flexibility and smoother transition of the blood vessel's pixels. It can be argued that the model can provide a more accurate vessel prediction.

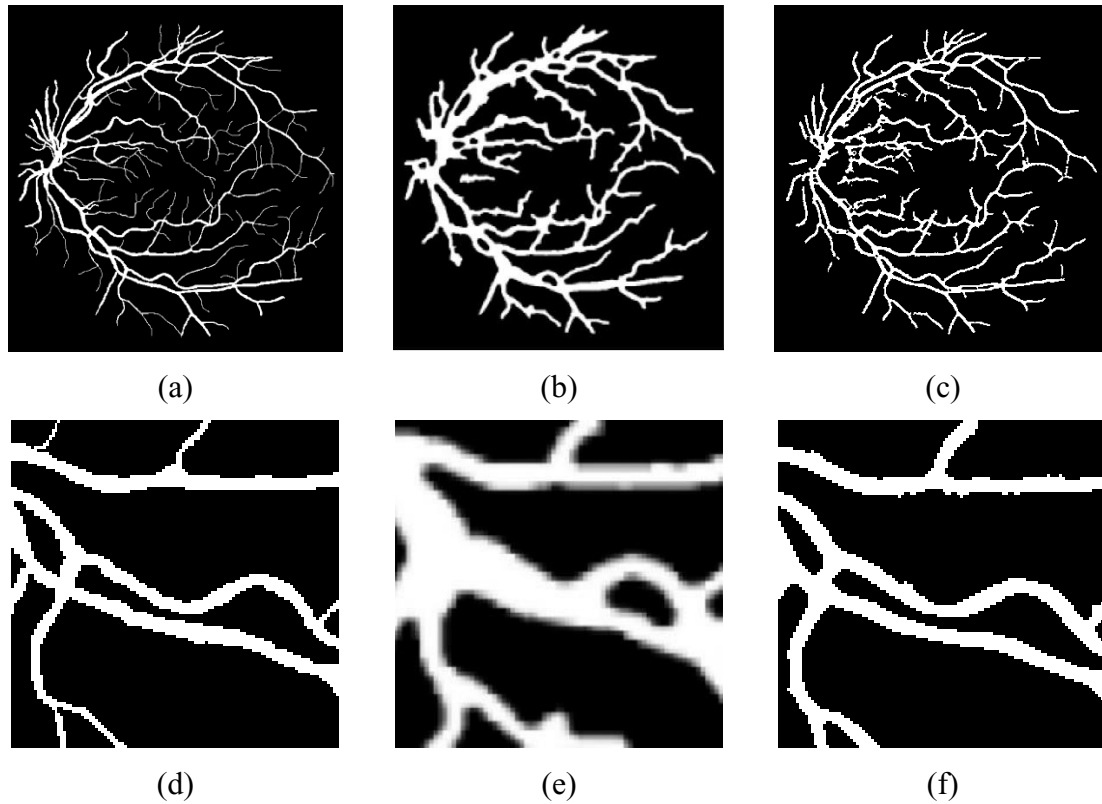


Figure 35: Comparison of the segmentation result by Orujov *et al.* [20] and the proposed method. Top row: (a) Ground Truth, (b) Segmentation result by [20], (c) Experimental result by the suggested model. Bottom row: The magnification of the top row

The higher sensitivity of [20] is debatable because the method overestimated the positive values by assigning more pixels to the vessels. On this basis, Table 5 compares the obtained Dice and Jaccard coefficients by [20] and the proposed model. According to the table, the suggested model has more shared pixels with the ground truth, which shows that the proposed technique is more similar to the manual delineations by the experts. In general, it should be pointed out that the current study suggests more flexibility in the determination of pixel classification, and it is more adapted to the input than [20] with fixed mean values for triangle membership functions.

TABLE 5: The performance comparison of [20] and the proposed model in terms of Dice and Jaccard indices

	<i>Dice</i>	<i>Jaccard</i>
Orujov <i>et al.</i> 2020 [20]	0.5500	0.3800
Proposed Model	0.7728	0.6298

Because the method of [20] used triangle membership functions, a faster execution time is expected due to their simplicity. According to the outcomes, the smoother Gaussian membership functions with non-zero trails resulted in more true positive pixels.

B. Yildirim (2015) [31] proposed the other fuzzy algorithm using mean and median features of the input and applied them to a type-1 fuzzy logic system. According to the reported results, the IT2 FS obtained better performance in terms of both sensitivity and accuracy. According to this report, the worst case is dedicated to image 3 with an accuracy of 92.72%. The suggested method obtained 93.84% on the same image.

K. Khatter *et al.* [57] used Robinson Compass Masks for the feature extraction step of their FCM algorithm. They utilized two pre-processing models and compared the results. According to their report, the accuracy of our proposed methodology outstands their obtained results on both methods, whereas sensitivity and specificity were not reported. The best result of this work has been acquired on the 19-th image with an accuracy of 0.9455 on their second methodology (combined response of Gaussian kernel and Gabor filter). However, the proposed model successfully obtained an accuracy of 0.9592 on the same image.

The method of Zana F. *et al.* (2001) [53] had the minor sensitivity among all evaluated works whose accuracy is below the proposed approach. Bankhead, Peter *et al.* (2012) [68] also stood under the current research results upon all measures.

Indeed, a higher accuracy value was obtained on the same data than the graph-based segmentation method proposed by Al Shehhi, Rasha *et al.* [65], while their sensitivity was higher. However, the authors mentioned that the algorithm's run-time is just 10 minutes, making it improper for on-site treatments.

The algorithm is also comparable with the work of Chaudhuri [46] as a method that applied matched filtering to segment the retinal blood vessels. The obtained accuracy shows that the proposed approach is not promising individually. Nevertheless, employing this method as a pre-processing step and combining that with the proposed IT2-FS resulted in higher accuracy and overall performance.

In general, and according to the results, it is noteworthy to say that the designed algorithm obtained the highest accuracy among the reviewed rule-based and unsupervised methods. Also, by evaluating the outcomes with supervised algorithms, it can be noted that the procedure effectively targets blood vessel segmentation and categorizes the retinal image pixels into vessel and background. Furthermore, comparing the results with the 2nd human observer, the method had a higher average accuracy with a slight degradation of sensitivity and specificity. This achievement means that the algorithm can replace with human expert segmentation. Figure 36 reports the best and worst segmentation cases in

terms of accuracy on the test samples of the DRIVE dataset. As observed, in the worst-case scenario, the algorithm has successfully segmented the blood vessels to a great extent in the optic disk area where several blood vessels meet, and the task of segmentation becomes challenging. As another example, a magnified view of the 11-th sample of DRIVE test data is illustrated in Figure 37.

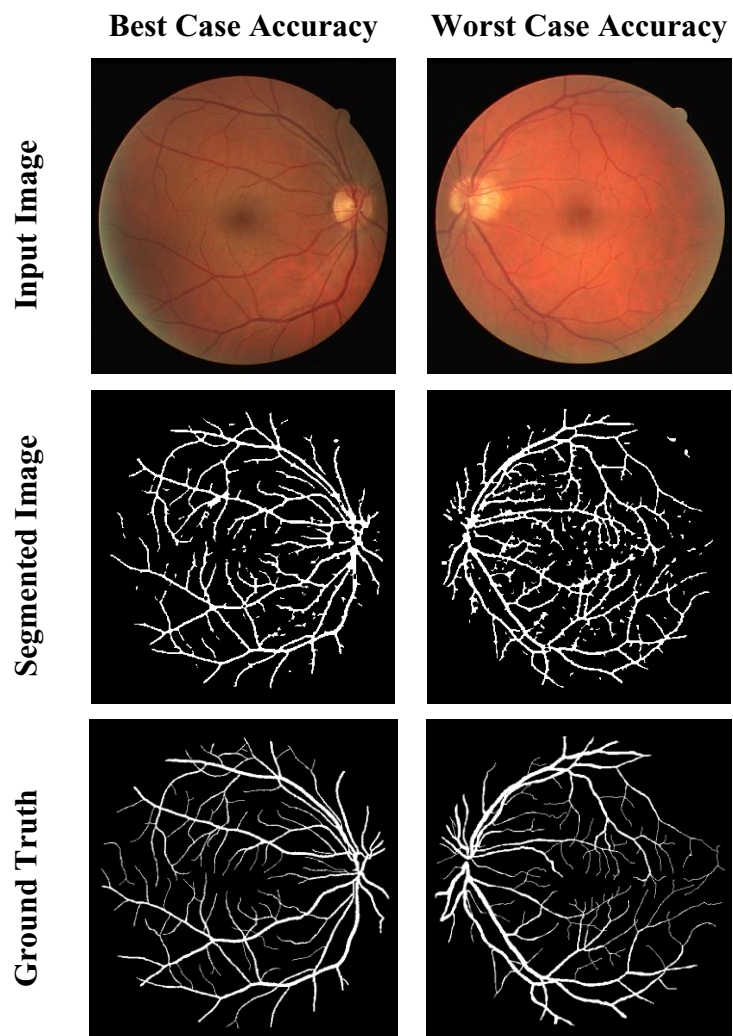


Figure 36: Segmentation results from the DRIVE test data

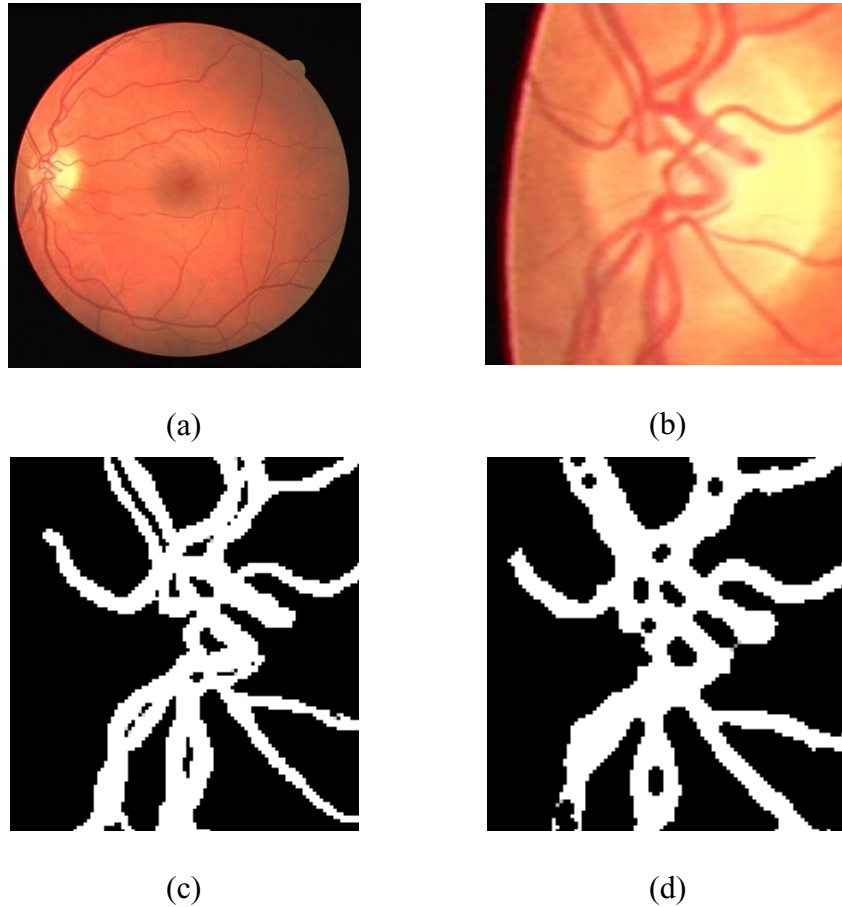


Figure 37: Detection of course vessels on an example from DRIVE test data (a) Original Color Image, (b) Magnified optic disk area, (c) Ground truth segmentation, (d) Predicted segmentation

According to Table 4, it can be realized that the average value of MSE is 0.0511, which is small enough to generate a difference between the ground truth and the processed image. The high value of PSNR shows promising and efficient results around the method's performance.

5.2. Summary of the work

This study is a new unsupervised and rule-based machine learning algorithm introducing a model based on interval type-2 fuzzy logic. The work uses various filters in pre-processing to improve the contrast between the blood vessels and the background. The steps include extracting the green channel of the RGB image, contrast enhancement using the CLAHE algorithm, removing background using median filter, smoothing the result by Gaussian filter, masking the FOV and highlighting the blood vessels using matched-template filtering. The features fed into the fuzzy logic system are extracted from Robinson Compact Masks in eight orientations, followed by taking the maximum of each pixel in the mirrored pairs to obtain four images with the highest value of these gradients. Interval type-2 fuzzy logic modelled the relationship between regions to segment the blood vessels.

In contrast, the uncertainties within the regions are estimated with the footprint of uncertainty. The Gaussian membership functions of the crisp inputs are dependent on the mean and sigma of the corresponding image, which makes the model adaptable to the gray tones of the input. The output of the fuzzy logic algorithm would be a grayscale image that mainly exposes the blood vessel edges. This crisp output is employed in the post-processing step to fill the gaps by morphological closing, and the binarized image is obtained using the hysteresis thresholding method. Finally, morphological erosion is used to remove the noise and shrink the vessels, and the unwanted noise has been removed by connected component analysis.

5.2. Strengths and Weaknesses

The novelty of the proposed method is to offer the interval type-2 fuzzy system as a new model that has not been widely studied in previously proposed methods. In this work, adaptable fuzzy membership functions were proposed by formulating the parameters of membership functions. This feature gives more freedom to the fuzzy algorithm to adjust the variables and handle the uncertainties based on the corresponding image. Furthermore, matched filtering has not been applied to the retinal blood vessels through pre-processing. At the same time, it has been realized that this method is beneficial by increasing the contrast of the blood vessels and delivering the lower noisy images to the fuzzy algorithm.

The algorithm has been validated using a publicly available DRIVE database. Experimental results indicate that the proposed method is efficient in detecting the retinal blood vessels from fundus images, and it can be positioned among the state-of-the-art methods.

Based on the acquired results, the algorithm can distinguish the blood vessels in the course regions, such as the optic disk area.

Interval type-2 fuzzy logic is a powerful tool that has been used in many real applications, and the proposed algorithm shows robust performance in detecting the target of blood vessels. The flexibility of the variables of fuzzy logic parameters and dynamic

rules makes this algorithm applicable in other medical image processing modalities or as an alternative for several deep learning applications.

A visual inspection of the segmented results reveals that the method has not covered all the sparse fine vessels. Besides, if the size of the lesions is comparable to blood vessels, they may not be entirely removed by the algorithm. This issue results in falsely detecting pixels as positive instances.

Although the designed algorithm is promising for pre-screening treatments, the average execution time of approximately 5 seconds makes it challenging for real-time applications. Although the proposed method outperforms many previous studies, this system is still missing smaller vessels with low contrast.

5.3. Future Work

The proposed method is one of the initial works in detecting the retinal blood vessels using the higher-order fuzzy inference system and, precisely, the IT2 FS. So, there is room for more improvement on the parameters of the fuzzy system and fuzzy rules.

In future surveys, the method's performance may improve by adding new features or linguistic rules to detect the low contrast and fine blood vessels. Indeed,

applying the algorithm to real-time applications demands reducing the processing time and requires more work on the fuzzy logic processing stage to optimize the runtime.

This work is only automating the segmentation of the retinal blood vessels. However, more work is required to help diagnose medical conditions.

Chapter 6: Conclusion

This thesis proposed a new automatic interval type-2 fuzzy logic algorithm to detect the retinal blood vessels in images acquired from a digital fundus camera. The manual diagnosis is performed by investigating the structure and patterns of retinal blood vessels in retina images. This task must be accomplished by particular expertise capable of identifying the vital biomarkers in the diagnostic process. This procedure is tedious and time-consuming when the number of data is large, and the grading is subject to error as it is highly dependent on the observer's experience. For this reason, carrying the retinal image analysis through a computer reduces the workload of ophthalmologists, for which automatic blood vessel segmentation would be the first and foremost step and is the objective of this study.

The newly introduced approach used some pre-processing steps, including matched filtering, to enhance the contrast of the blood vessels. The inputs of the proposed algorithm

are extracted from the gradient features in eight orientations. As far as is known, the application of interval type-2 fuzzy system on the segmentation of retinal blood vessels is a task that has been surveyed in only one article. Using adaptive values for the parameters of the membership functions is a novel approach in designing the fuzzy algorithm for retinal blood vessels that can make the algorithm more practical on actual data. Such proposed techniques tackled the drawbacks of the currently-published model by providing more similar segmented images with the ground truth with a higher Jaccard index. By evaluating the results with the current studies, it can be argued that 94.89% accuracy obtained by the method was competent and achieved promising results for the application of retinal image computer analysis.

References

- [1] T. H. Farag, W. A. Hassan, H. A. Ayad, A. S. AlBahussain, U. A. Badawi, & M. K. Alsmadi “Extended Absolute Fuzzy Connectedness Segmentation Algorithm Utilizing Region and Boundary-Based Information.” *Arabian Journal for Science and Engineering* (2011), vol. 42, no. 8, Springer Berlin Heidelberg, 2017, pp. 3573–83.
- [2] Sonka, M., Hlavac, V., & Boyle, R. “Image Processing, Analysis, and Machine Vision.” 3rd ed., Thompson Learning, 2008.
- [3] Surya Prabha, D., and J. Satheesh Kumar. “Performance Evaluation of Image Segmentation Using Objective Methods.” *Indian Journal of Science and Technology*, vol. 9, no. 8, 2016.
- [4] Herman, Gabor T, T. Yung Kong, and Krzysztof Chris Ciesielski. “Fuzzy Connectedness Segmentation: A Brief Presentation of the Literature.” *Combinatorial Image Analysis*. Cham: Springer International Publishing, 2016. 21–30. Web.
- [5] Udupa, Jayaram K., and Supun Samarasekera. “Fuzzy Connectedness and Object Definition: Theory, Algorithms, and Applications in Image Segmentation.” *Graphical Models and Image Processing*, vol. 58, no. 3, Elsevier Inc, 1996, pp. 246–61.

- [6] P.K. Saha and J.K. Udupa. "Fuzzy connected object delineation: axiomatic path strength definition and the case of multiple seeds." *Computer Vision and Image Understanding*, 83:275–295, 2001.
- [7] Maedeh Rasoulzadeh, GholamReza Ardeshir Behrastaghi, "Extraction of Blood vessels in X-Ray Angiography Image Using Fuzzy Logic". *International Journal of Advanced Research in Computer Science*, Vol 1, No 3,2010
- [8] Chaira, Tamalika., and Ajoy K. Ray. "Fuzzy Image Processing and Applications with MATLAB." CRC Press/Taylor & Francis, 2010.
- [9] Cintula, Petr, Christian G. Fermüller, and Carles Noguera, "Fuzzy Logic", *The Stanford Encyclopedia of Philosophy* (Fall 2017 Edition), Edward N. Zalta (ed.),
- [10] Melin, Gonzalez, C. I., Castro, J. R., Mendoza, O., & Castillo, O. "Edge-Detection Method for Image Processing Based on Generalized Type-2 Fuzzy Logic." *IEEE Transactions on Fuzzy Systems*, vol. 22, no. 6, IEEE, 2014, pp. 1515–25.
- [11] O. Mendoza, P. Melin and G. Licea, "A New Method for Edge Detection in Image Processing Using Interval Type-2 Fuzzy Logic," 2007 IEEE International Conference on Granular Computing (GRC 2007), 2007, pp. 151-151.
- [12] R. Gonzalez and R. Woods, "Digital Image Processing", Addison Wesley, 1992, pp 414 - 428.
- [13] Ashoorirad, M., and R. Baghbani. "Blood Vessel Segmentation in Angiograms Using Fuzzy Inference System and Mathematical Morphology." 2009 International

Conference on Signal Processing Systems, IEEE, 2009, pp. 272–76,
doi:10.1109/ICSPS.2009.46.

- [14] Castillo, Oscar; Amador-Angulo, Leticia; Castro, Juan R; Garcia-Valdez, Mario “A Comparative Study of Type-1 Fuzzy Logic Systems, Interval Type-2 Fuzzy Logic Systems and Generalized Type-2 Fuzzy Logic Systems in Control Problems.” *Information Sciences*, vol. 354, Elsevier Inc, 2016, pp. 257–74.
- [15] Claudia I Gonzalez; Patricia Melin; Oscar Castillo “Edge Detection Method Based on General Type-2 Fuzzy Logic Applied to Color Images.” *Information (Basel)*, vol. 8, no. 3, MDPI AG, 2017, p. 104.
- [16] Abdallah A. Alshennawy, and Ayman A. Aly. “Edge Detection in Digital Images Using Fuzzy Logic Technique” *World Academy of Science, Engineering and Technology* 51, 2009
- [17] Mendoza, Olivia, Patricia Melin, and Guillermo Licea. “Interval Type-2 Fuzzy Logic for Edges Detection in Digital Images.” *International Journal of Intelligent Systems*, vol. 24, no. 11, Wiley Subscription Services, Inc., A Wiley Company, 2009, pp. 1115–33.
- [18] Melin, Patricia, Olivia Mendoza, and Oscar Castillo. “An Improved Method for Edge Detection Based on Interval Type-2 Fuzzy Logic.” *Expert Systems with Applications*, vol. 37, no. 12, Elsevier Ltd, 2010, pp. 8527–35.

- [19] Melin, Patricia, Olivia Mendoza, and Oscar Castillo. "An Improved Method for Edge Detection Based on Interval Type-2 Fuzzy Logic." *Expert systems with applications* 37, no. 12 (2010): 8527–8535.
- [20] Orujov, F, R Maskeliūnas, R Damaševičius, and W Wei. "Fuzzy Based Image Edge Detection Algorithm for Blood Vessel Detection in Retinal Images." *Applied Soft Computing*, vol. 94, Elsevier B.V, 2020, p. 106452.
- [21] Zuiderveld, Karel. "Contrast Limited Adaptive Histogram Equalization." *Graphic Gems IV*. San Diego: Academic Press Professional, 1994. 474–485
- [22] Kaur, Kiranpreet ; Mutenja, Vikram; Gill, Inderjeet Singh. "Fuzzy Logic Based Image Edge Detection Algorithm in MATLAB." *International Journal of Computer Applications*, vol. 1, no. 22, 2010, pp. 57–60.
- [23] Mandeep Singh Sandhu Er. Vikram Mutneja, Er. Nishi. "Image Edge Detection by Using Rule Based Fuzzy Classifier." (IJCSIT) *International Journal of Computer Science and Information Technologies*, Vol. 2 (5), 2011, 2434-2439
- [24] Haq, Izhar ; Anwar, Shahzad ; Shah, Kamran ; Khan, Muhammad Tahir ; Shah, Shaukat Ali; Coles, Jonathan. "Fuzzy Logic Based Edge Detection in Smooth and Noisy Clinical Images." *PloS One*, vol. 10, no. 9, Public Library of Science, 2015, pp. e0138712–e0138712.
- [25] Raheja, Sahil, and Akshi Kumar. "Edge Detection Based on Type-1 Fuzzy Logic and Guided Smoothing." *Evolving Systems*, vol. 12, no. 2, 2021, pp. 447–62.

- [26] Bibiloni, Pedro, Manuel González-Hidalgo, and Sebastia Massanet. "A Real-Time Fuzzy Morphological Algorithm for Retinal Vessel Segmentation." *Journal of Real-Time Image Processing*, vol. 16, no. 6, Springer Berlin Heidelberg, 2019, pp. 2337–50.
- [27] Khan, Nafis uddin, and K. V. Arya. "A New Fuzzy Rule Based Pixel Organization Scheme for Optimal Edge Detection and Impulse Noise Removal." *Multimedia Tools and Applications*, vol. 79, no. 45-46,.
- [28] H. C. Lee, "Fuzzy Logic-based Binarization: A Divide and Conquer Approach," *International Information Institute (Tokyo). Information*, vol. 21, (2), pp. 687-694, 2018.
- [29] LANDINI, G, D.A RANDELL, S FOUAD, and A GALTON. "Automatic Thresholding from the Gradients of Region Boundaries: AUTOMATIC THRESHOLDING." *Journal of Microscopy (Oxford)*, vol. 265, no. 2, 2017, pp. 185–95.
- [30] Rafael C. Gonzalez, Richard Eugene Woods, Steven L. Eddins, "Digital Image Processing Using MATLAB," 2nd end. Pearson Education, 2004
- [31] B. Yildirim, "Segmentation of Retinal Blood Vessels Using A Novel Fuzzy Logic Algorithm," M.S. Thesis, University of Bridgeport, Connecticut, USA, 2015
- [32] Medina-Carnicer, R., Muñoz-Salinas, R., Yeguas-Bolivar, E., & Diaz-Mas, L. "A Novel Method to Look for the Hysteresis Thresholds for the Canny Edge Detector." *Pattern Recognition*, vol. 44, no. 6, Elsevier Ltd, 2011, pp. 1201–11.

- [33] T. Kauppi, V. Kalesnykiene, J. Kamarainen, L. Lensu, and I. Sorri, "DIARETDB0: Evaluation Database and Methodology for Diabetic Retinopathy Algorithms," Mach. Vis. Pattern Recognit. Res. Group, Lappeenranta Univ. Technol. Finland., pp. 1–17, 2006.
- [34] Tomi Kauppi, Valentina Kalesnykiene, Joni-Kristian Kamarainen, Lasse Lensu, Iris Sorri, Asta Raninen, Raija Voutilainen, Hannu Uusitalo, Heikki K"alvi"ainen and Juhani Pietil"a "DIARETDB1: diabetic retinopathy database and evaluation protocol," in Proceedings of the British Machine Vision Conference 2007, 2007, p. 15.1-15.10.
- [35] R. Afrin and P. C. Shill, "Automatic Lesions Detection and Classification of Diabetic Retinopathy Using Fuzzy Logic," 2019 International Conference on Robotics,Electrical and Signal Processing Techniques (ICREST), 2019, pp. 527-532.
- [36] DeHoog, Edward, and James Schwiegerling. "Fundus Camera Systems: a Comparative Analysis." Applied Optics. Optical Technology and Biomedical Optics, vol. 48, no. 2, Optical Society of America, 2009, pp. 221–28.
- [37] C. P. Wilkinson, Frederick L. Ferris, Ronald E. Klein, Paul P. Lee, Carl David Agardh, Matthew Davis, Diana Dills, Anselm Kampik, R. Pararajasegaram, and Juan T. Verdaguer. "Proposed international clinical diabetic retinopathy and diabetic macular edema disease severity scales." Ophthalmology, 10(9):1677–1682, September 2003.

- [38] Kromer, Robert ; Shafin, Rahman ; Boelefahr, Sebastian ; Klemm, Maren. "An Automated Approach for Localizing Retinal Blood Vessels in Confocal Scanning Laser Ophthalmoscopy Fundus Images." *Journal of Medical and Biological Engineering*, vol. 36, no. 4, Springer Nature B.V, 2016, pp. 485–94.
- [39] Gagnon, Langis, Marc Lalonde, Mario Beaulieu, and Marie-Carole Boucher. "Procedure to detect anatomical structures in optical fundus images." *Medical Imaging 2001. International Society for Optics and Photonics*, (2001): 1218-1225.
- [40] Leung, H., Wang, J. J., Rochtchina, E., Tan, A. G., Wong, T. Y., Klein, R., Hubbard, L. D., & Mitchell, P. "Relationships Between Age, Blood Pressure, and Retinal Vessel Diameters in an Older Population." *Investigative Ophthalmology & Visual Science*, vol. 44, no. 7, ARVO, 2003, pp. 2900–04.
- [41] Staal, J, M.D Abramoff, M Niemeijer, M.A Viergever, and B van Ginneken. "Ridge-Based Vessel Segmentation in Color Images of the Retina." *IEEE Transactions on Medical Imaging*, vol. 23, no. 4, IEEE, 2004, pp. 501–09.
- [42] Sinthanayothin, Chanjira, James F. Boyce, Helen L. Cook, and Thomas H. Williamson. "Automated localisation of the optic disc, fovea, and retinal blood vessels from digital color fundus images." *British Journal of Ophthalmology* 83.8 (1999): 902-910.
- [43] Ricci, Elisa, and Renzo Perfetti. "Retinal blood vessel segmentation using line operators and support vector classification." *Medical Imaging, IEEE Transactions on* 26.10 (2007): 1357-1365.

- [44] Research Section, Digital Retinal Image for Vessel Extraction, (DRIVE) Database. Utrecht, the Netherlands, Univ., Med. Center Utrecht, Image Sci. Inst. [Online]. Available: <http://www.isi.uu.nl/Research/Databases/DRIVE>
- [45] Dutta, Tapash, Nilanjan Dutta, and Oishila Bandyopadhyay “Retinal Blood Vessel Segmentation and Bifurcation Point Detection.” *Combinatorial Image Analysis*, Springer International Publishing, 2016, pp. 261–75.
- [46] Chaudhuri, S; Chatterjee, S; Katz, N; Nelson, M; Goldbaum, M “Detection of Blood Vessels in Retinal Images Using Two-Dimensional Matched Filters.” *IEEE Transactions on Medical Imaging*, vol. 8, no. 3, IEEE, 1989, pp. 263–69.
- [47] Kumar, Kundan, Debashisa Samal, and Suraj. “Automated Retinal Vessel Segmentation Based on Morphological Pre-processing and 2D-Gabor Wavelets.” *Advanced Computing and Intelligent Engineering*, Springer Singapore, 2020, pp. 411–23.
- [48] da Rocha, Douglas Abreu, Ana Beatriz Lordeiro Barbosa, Daniela Silva Guimarães, Leonardo Miranda Gregório, Luiz Henrique Nacife Gomes, Luciana da Silva Amorim, and Zélia Myriam Assis Peixoto. “An Unsupervised Approach to Improve Contrast and Segmentation of Blood Vessels in Retinal Images Using CLAHE, 2D Gabor Wavelet, and Morphological Operations.” *Research on Biomedical Engineering*, vol. 36, no. 1, 2020, pp. 67–75.
- [49] Fraz, Muhammad Moazam; Remagnino, Paolo; Hoppe, Andreas; Uyyanonvara, Bunyarit; Rudnicka, Alicja R; Owen, Christopher G; Barman, Sarah A “An

- Ensemble Classification-Based Approach Applied to Retinal Blood Vessel Segmentation.” IEEE Transactions on Biomedical Engineering, vol. 59, no. 9, IEEE, 2012, pp. 2538–48.
- [50] Liskowski, Pawel, and Krzysztof Krawiec. “Segmenting Retinal Blood Vessels With Deep Neural Networks.” IEEE Transactions on Medical Imaging, vol. 35, no. 11, IEEE, 2016, pp. 2369–80.
- [51] A. Lahiri, A. G. Roy, D. Sheet and P. K. Biswas, "Deep neural ensemble for retinal vessel segmentation in fundus images towards achieving label-free angiography," 2016 38th Annual International Conference of the IEEE Engineering in Medicine and Biology Society (EMBC), 2016, pp. 1340-1343.
- [52] Soares, J.V.B; Leandro, J.J.G; Cesar, R.M; Jelinek, H.F; Cree, M.J. “Retinal Vessel Segmentation Using the 2-D Gabor Wavelet and Supervised Classification.” IEEE Transactions on Medical Imaging, vol. 25, no. 9, IEEE, 2006, pp. 1214–22.
- [53] Zana, F., and J. C. Klein. “Segmentation of Vessel-Like Patterns Using Mathematical Morphology and Curvature Evaluation.” IEEE Transactions on Image Processing, vol. 10, no. 7, IEEE, 2001, pp. 1010–19.
- [54] Mendel, Jerry M., Hani Hagra, Woei-Wan Tan, William W. Melek, and Hao Ying. Introduction to Type-2 Fuzzy Logic Control: Theory and Applications. Hoboken, New Jersey: IEEE Press, John Wiley & Sons, 2014.
- [55] Figueroa, Juan Carlos. “On the Fuzzy Extension Principle for LP Problems with Interval Type-2 Technological Coefficients.” Ingeniería (Bogotá, Colombia :

- 1993), vol. 20, no. 1, Universidad Distrital Francisco José de Caldas, 2015, pp. 101–10.
- [56] Martínez, Gabriela E ; Gonzalez, Claudia I ; Mendoza, Olivia ; Melin, Patricia. “General Type-2 Fuzzy Sugeno Integral for Edge Detection.” *Journal of Imaging*, vol. 5, no. 8, MDPI AG, 2019, p. 71.
- [57] K. Khatter, D. Relan and A. Mishra, "Retinal Vessel Segmentation using Robinson Compass Mask and Fuzzy C-Means," 2020 IEEE 17th India Council International Conference (INDICON), 2020, pp. 1-6.
- [58] Dongrui Wu, and J.Mendel. “Enhanced Karnik--Mendel Algorithms.” *IEEE Transactions on Fuzzy Systems*, vol. 17, no. 4, IEEE, 2009, pp. 923–34.
- [59] Oloumi, Faraz, author.; Rangayyan, Rangaraj M., author.; Ells, Anna L., author. “Digital Image Processing for Ophthalmology: Detection and Modeling of Retinal Vascular Architecture.” Morgan & Claypool Publishers, 2014.
- [60] Møller, Aage R. *Sensory Systems : Anatomy and Physiology*. Academic Press, 2003.
- [61] Fitzgerald, Barry W. “Using Hawkeye from the Avengers to Communicate on the Eye.” *Advances in Physiology Education*, vol. 42, no. 1, 2018, pp. 90–98.
- [62] Peter J. Watkins, Stephanie A. Amiel, Simon L. Howell, Eileen Turner. *Diabetes and Its Management*. 6th ed., Blackwell Science, 2003.
- [63] The Vitreous, Macula, and Retina (VMR) Institute, “Diabetic Retinopathy Treatment in California,” Vitreous, Macula, and Retina (VMR) Institute, [Online].

Available:<https://www.vmrinstitute.com/what-is-diabetic-retinopathy/> [Accessed: 2020]

- [64] Fraz, M.M ; Remagnino, P ; Hoppe, A ; Uyyanonvara, B ; Rudnicka, A.R ; Owen, C.G ; Barman, S.A “Blood Vessel Segmentation Methodologies in Retinal Images – A Survey.” *Computer Methods and Programs in Biomedicine*, vol. 108, no. 1, Elsevier Ireland Ltd, 2012, pp. 407–33.
- [65] Al Shehhi, Rasha; Marpu, Prashanth Reddy; Woon, Wei Lee; Zaldivar, Daniel. “An Automatic Cognitive Graph-Based Segmentation for Detection of Blood Vessels in Retinal Images.” *Mathematical Problems in Engineering*, vol. 2016, Hindawi Publishing Corporation, 2016, pp. 1–15.
- [66] Marín, D; Aquino, A; Gegundez-Arias, M E; Bravo, J M. “A New Supervised Method for Blood Vessel Segmentation in Retinal Images by Using Gray-Level and Moment Invariants-Based Features.” *IEEE Transactions on Medical Imaging*, vol. 30, no. 1, IEEE, 2011, pp. 146–58.
- [67] Tolia, Y., and S. Panas. “A Fuzzy Vessel Tracking Algorithm for Retinal Images Based on Fuzzy Clustering.” *IEEE Transactions on Medical Imaging*, vol. 17, no. 2, IEEE, 1998, pp. 263–73.
- [68] Bankhead, Peter; Scholfield, C Norman; McGeown, J Graham; Curtis, Tim M; Serrano-Gotarredona, Teresa. “Fast Retinal Vessel Detection and Measurement Using Wavelets and Edge Location Refinement.” *PloS One*, vol. 7, no. 3, Public Library of Science, 2012, pp. e32435–e32435.

- [69] Almaraashi, M., John, R., Hopgood, A., & Ahmadi, S. "Learning of Interval and General Type-2 Fuzzy Logic Systems Using Simulated Annealing: Theory and Practice." *Information Sciences*, vol. 360, Elsevier Inc, 2016, pp. 21–42.
- [70] Castillo, O.; Sanchez, M.A.; Gonzalez, C.I.; Martinez, G.E. Review of Recent Type-2 Fuzzy Image Processing Applications. *Information* 2017, 8, 97.
- [71] Duda, Richard O., Peter E. Hart, and David G. Stork. *Pattern Classification*. 2nd ed. New York: Wiley, 2001. Print.
- [72] Friedman, D. H.. "Detection of signals by template matching." Baltimore, MD: John Hopkins University, Press, 1969
- [73] Banerjee, S.; Sule Ercetin, S.; Tekin, A. (Eds.), "Chaos Theory in Politics." X, 201 p.13, 2014
- [74] Mitiku T, Manshahia MS. Neuro fuzzy inference approach: a survey. *Int JS Res Sci. Engg. Tech.* 2018 Mar;4(7):505-19.
- [75] Hosseini, Rahil, Tim Ellis, Mahdi Mazinani, and J. Dehmeshki. "A genetic fuzzy approach for rule extraction for rule-based classification with application to medical diagnosis." In *European Conference on Machine Learning and Principles and Practice of Knowledge Discovery in Databases (ECML PKDD)*, pp. 05-09. 2011.
- [76] Meindert Niemeijer, Joes Staal, Bram van Ginneken, Marco Loog, Michael D. Abramoff, "Comparative study of retinal vessel segmentation methods on a new

publicly available database," Proc. SPIE 5370, Medical Imaging 2004: Image Processing

Appendix

Appendix 1: Methodology MATLAB Code

Reading image

```
I_int = imread('01_test.tif');  
ref = imread('01_manual1.gif');
```

Pre-processing

Green Channel Extraction

```
I_green = I_int(:,:,2);
```

Contrast-limited adaptive histogram equalization (CLAHE)

```
I_Hist = adapthisteq(I_green,'NumTiles',[9 9],'ClipLimit',  
0.02,'Distribution','rayleigh');
```

Median filtering and BG removal

```
I_Med = medfilt2(I_Hist,[45 45]);  
Im_sub = imsubtract(I_Med,I_Hist);
```

Gaussian Blur

```
sigma = std2(Im_sub);  
Im_Gauss = imgaussfilt(Im_sub, sigma,'FilterDomain','spatial','FilterSize',3);
```

Retina Area Extraction

```
Luminance = 0.2989*I_int(:,:,1)+0.5870*I_int(:,:,2)+0.1140*I_int(:,:,3);  
mean_val = mean2(Luminance);  
[m, n] = size(Luminance);  
mask = Luminance;  
for i = 1:m
```

```

for j = 1:n
    if mask(i,j) > mean_val
        mask(i,j) = 1;
    else
        mask(i,j) = 0;
    end
end
end
end
% Morphological Closing
se = strel('disk',6);
mask_close = imclose(mask,se);
Im_Gauss(~mask_close) = 0;

```

Matched Filtering

```

Im_filt = im2double(Im_Gauss);

sig = 1.5; %sigma
L = 7; % length
Theta = 0:15:180; % different rotations

matched_filt = zeros(size(Im_filt));

p = max(ceil(3*sig),(L-1)/2);
[x,y] = meshgrid(-p:p,-p:p); % non-rotated coordinate system
for t = Theta
    t = t / 180 * pi; % changing the angle into radian
    u = cos(t)*x - sin(t)*y; % rotated coordinate system
    v = sin(t)*x + cos(t)*y; % rotated coordinate system
    N = (abs(u) <= 3*sig) & (abs(v) <= L/2); % Defining a neighborhood N
    k = exp(-u.^2/(2*sig.^2)); % the weights in each kernel
    k = k - mean(k(N)); % the convolutional mask used in matched filter
    % is the result of subtracting its mean value from the kernel itself
    k(~N) = 0; % set kernel outside of domain to 0

    K_prim = conv2(Im_filt,k,'same');
    matched_filt = max(matched_filt,K_prim);
end

matched_filt = matched_filt/max(matched_filt(:)); % force output to be in [0,1] interval

```

Defining 8-direction gradients

```

kernel_0 = [-1 -2 -1;0 0 0;1 2 1];
G_0 = conv2(matched_filt,kernel_0,'same');

```

```

kernel_180 = [1 2 1;0 0 0;-1 -2 -1];
G_180 = conv2(matched_filt, kernel_180, 'same');

kernel_45 = [-2 -1 0;-1 0 1;0 1 2];
G_45 = conv2(matched_filt, kernel_45, 'same');

kernel_225 = [2 1 0;1 0 -1;0 -1 -2];
G_225 = conv2(matched_filt, kernel_225, 'same');

kernel_90 = [-1 0 1;-2 0 2;-1 0 1];
G_90 = conv2(matched_filt, kernel_90, 'same');

kernel_270 = [1 0 -1;2 0 -2;1 0 -1];
G_270 = conv2(matched_filt, kernel_270, 'same');

kernel_135 = [0 1 2;-1 0 1;-2 -1 0];
G_135 = conv2(matched_filt, kernel_135, 'same');

kernel_315 = [0 -1 -2;1 0 -1;2 1 0];
G_315 = conv2(matched_filt, kernel_315, 'same');

```

Picking the largest value of gradients

```

I_X = zeros(size(matched_filt));
for M = 1:m
    for N = 1:n
        I_X(M,N) = max(G_0(M,N), G_180(M,N));
    end
end

I_Z = zeros(size(matched_filt));
for M = 1:m
    for N = 1:n
        I_Z(M,N) = max(G_45(M,N), G_225(M,N));
    end
end

I_Y = zeros(size(matched_filt));
for M = 1:m
    for N = 1:n
        I_Y(M,N) = max(G_90(M,N), G_270(M,N));
    end
end

I_K = zeros(size(matched_filt));
for M = 1:m
    for N = 1:n

```

```

        I_K(M,N) = max(G_135(M,N),G_315(M,N));
    end
end

```

FIS Design

```

low_1 = min(I_X(:)); % input I_X
high_1 = max(I_X(:));
medium_1 = (high_1 - low_1)/2;
sigma_1 = (high_1)/5;

% input I_Y
low_2 = min(I_Y(:));
high_2 = max(I_Y(:));
medium_2 = (high_2 - low_2)/2;
sigma_2 = (high_2)/5;

% input I_Z
low_3 = min(I_Z(:));
high_3 = max(max(I_Z));
medium_3 = (high_3 - low_3)/2;
sigma_3 = (high_3)/5;

% input I_K
low_4 = min(I_K(:));
high_4 = max(I_K(:));
medium_4 = (high_4 - low_4)/2;
sigma_4 = (high_4)/5;

fis = mamfistype2('Name', "EdgeDetection", 'TypeReductionMethod', "ekm");

fis = addInput(fis,[0 6 ],'Name','I_X');
fis = addInput(fis,[0 6 ],'Name','I_Y');
fis = addInput(fis,[0 6 ],'Name','I_Z');
fis = addInput(fis,[0 6 ],'Name','I_K');

fis = addMF(fis, "I_X", "gausmf",[sigma_1
low_1], 'LowerScale',0.9, 'LowerLag',0.09, 'Name', 'Low');
fis = addMF(fis, "I_X", "gausmf",[sigma_1
medium_1], 'LowerScale',0.9, 'LowerLag',0.09, 'Name', 'Medium');
fis = addMF(fis, "I_X", "gausmf",[sigma_1
high_1], 'LowerScale',0.9, 'LowerLag',0.09, 'Name', 'High');

fis = addMF(fis, "I_Y", "gausmf",[sigma_2
low_2], 'LowerScale',0.9, 'LowerLag',0.09, 'Name', 'Low');
fis = addMF(fis, "I_Y", "gausmf",[sigma_2
medium_2], 'LowerScale',0.9, 'LowerLag',0.09, 'Name', 'Medium');

```

```

fis = addMF(fis, "I_Y", "gaussmf", [sigma_2
high_2], 'LowerScale', 0.9, 'LowerLag', 0.09, 'Name', 'High');

fis = addMF(fis, "I_Z", "gaussmf", [sigma_3
low_3], 'LowerScale', 0.9, 'LowerLag', 0.09, 'Name', 'Low');
fis = addMF(fis, "I_Z", "gaussmf", [sigma_3
medium_3], 'LowerScale', 0.9, 'LowerLag', 0.09, 'Name', 'Medium');
fis = addMF(fis, "I_Z", "gaussmf", [sigma_3
high_3], 'LowerScale', 0.9, 'LowerLag', 0.09, 'Name', 'High');

fis = addMF(fis, "I_K", "gaussmf", [sigma_4
low_4], 'LowerScale', 0.9, 'LowerLag', 0.09, 'Name', 'Low');
fis = addMF(fis, "I_K", "gaussmf", [sigma_4
medium_4], 'LowerScale', 0.9, 'LowerLag', 0.09, 'Name', 'Medium');
fis = addMF(fis, "I_K", "gaussmf", [sigma_4
high_4], 'LowerScale', 0.9, 'LowerLag', 0.09, 'Name', 'High');
% Fuzzy output
fis = addOutput(fis, [0 1], 'Name', 'output');
% Gaussian MF
fis = addMF(fis, "output", "gaussmf", [1/4
1], 'LowerScale', 0.9, 'LowerLag', 0.09, 'Name', 'Edge');
fis = addMF(fis, "output", "gaussmf", [1/4 0], 'LowerScale', 0.9, 'LowerLag', 0.09, 'Name', 'No-
Edge');

RuleList = [3 3 3 3 1 1 2; 2 2 2 2 1 1 2; 1 1 1 1 2 1 1];
fis = addRule(fis, [RuleList]);
fis.Rules

% Defuzzification
Ieval = zeros(size(matched_filt));

for ii = 1:size(matched_filt,1)
    Ieval(ii,:) = evalfis(fis, [(I_X(ii,:)); (I_Y(ii,:)); (I_Z(ii,:)); (I_K(ii,:))]);
end

```

Hysteresis Thresholding

```

Im_rescale = rescale(Ieval); %pushing back the histogram to zero
imhist(Im_rescale)
Thresh1 = 0.05;
Thresh2 = 0.045;
lower_thresh = Im_rescale > Thresh2; % Detect Edge points above lower limit
[upper_thresh_x, upper_thresh_y] = find(Im_rescale > Thresh1); % finding the coordinates
of edges above upper threshold
bw = bwselect(lower_thresh, upper_thresh_y, upper_thresh_x, 8); % extract all connected
regions in lower_thresh
% that includes a point that has a value above Thresh1

```

processing binary image

Morphological Closing

```
se1 = strel('disk',1);
Im_close = imclose(bw,se1);

% Morphological Erosion
se2 = strel('square',3); %try 'square', 3
Im_erode = imerode (Im_close,se2);
```

Connected Component Analysis

```
cc = bwconncomp(Im_erode,8);
numPixels = cellfun(@numel,cc.PixelIdxList);

idx = find(numPixels<10);
[f,sig] = size(idx);
for z = 1:sig
    Index = idx(1,z);
    Im_erode(cc.PixelIdxList{Index}) = 0;
end
```